

From Pixels to Places: A Systematic Benchmark for Evaluating Image Geolocalization Ability in Large Language Models

Lingyao Li*
University of South Florida
Tampa, USA

Runlong Yu*
University of Alabama
Tuscaloosa, USA

Qikai Hu
University of Michigan
Ann Arbor, USA

Bowei Li
Texas Tech University
Lubbock, USA

Min Deng
Texas Tech University
Lubbock, USA

Yang Zhou
Texas A & M University
College Station, USA

Xiaowei Jia
University of Pittsburgh
Pittsburgh, USA

Abstract

Image geolocalization, the task of identifying the geographic location depicted in an image, is important for applications in crisis response, digital forensics, and location-based intelligence. While recent advances in large language models (LLMs) offer new opportunities for visual reasoning, their ability to perform image geolocalization remains underexplored. In this study, we introduce a benchmark called **IMAGEO-Bench** that systematically evaluates accuracy, distance error, geospatial bias, and reasoning process. Our benchmark includes three diverse datasets covering global street scenes, points of interest (POIs) in the United States, and a private collection of unseen images. Through experiments on 10 state-of-the-art LLMs, including both open- and closed-source models, we reveal clear performance disparities, with closed-source models generally showing stronger reasoning. Importantly, we uncover geospatial biases as LLMs tend to perform better in high-resource regions (e.g., North America, Western Europe, and California) while exhibiting degraded performance in underrepresented areas. Regression diagnostics demonstrate that successful geolocalization is primarily dependent on recognizing urban settings, outdoor environments, street-level imagery, and identifiable landmarks. Overall, **IMAGEO-Bench** provides a rigorous lens into the spatial reasoning capabilities of LLMs and offers implications for building geolocation-aware AI systems.

Datasets: <https://doi.org/10.5281/zenodo.16670471>

Code: <https://github.com/Lingyao1219/benchmark-reverse-geocoding>

1 Introduction

Image geolocalization, the process of inferring geographic coordinates or addresses from visuals, presents a complex challenge at the intersection of computer vision and geographic information systems (GIS) [15, 24, 39, 47]. Image geolocalization requires holistic scene interpretation and reasoning, encompassing both explicit indicators (e.g., landmarks, signage) and contextual cues (e.g., architectural styles, vegetation, spatial layout) to infer a precise location [24, 40]. The accurate identification of location from images has important implications for real-world scenarios, including digital forensics [16], urban analytics [24] and crisis management [19, 46].

Conventionally, this task has been investigated with computer vision models, using either supervised classification [26, 29] or retrieval-based methods [30, 34, 35, 50]. These models often leverage metadata embedded in image files [28] or rely on extensive

GIS databases [2, 9] to recognize landmark or visual cues. However, early methods often fail to generalize to previously unseen environments and perform inadequately in the absence of distinctive landmarks. Their effectiveness is further constrained by data coverage and resolution, especially when the metadata is missing.

Recent advances in large language models (LLMs), such as GPT and Gemini, have transformed the landscape of image understanding and spatial reasoning [4, 21, 32, 41]. These models can describe intricate details, understand spatial relationships between objects, and infer context from subtle visual cues within an image [4, 44]. By leveraging extensive world knowledge and visual-textual alignment, LLMs offer a promising avenue for overcoming the limits of conventional geolocalization, even when confronted with out-of-distribution data [22, 42, 49]. Recent research further demonstrates that targeted strategies, such as supervised fine-tuning [45] and retrieval-augmented inference [22], can substantially enhance LLMs’ geolocalization capabilities.

In parallel with LLM advances, there has been rapid progress in developing benchmarks to evaluate their visual and linguistic capabilities [6, 12, 18]. A representative example is GEO-Bench, which evaluates LLMs on classification and segmentation tasks in geoscience [18]. For image geolocalization, benchmarks like Img2Loc [49] and LLMGeo [36] have assessed LLMs’ ability to localize images. However, these efforts often rely on established datasets and lag in incorporating the recent model advances. Moreover, key dimensions like LLMs’ spatial reasoning abilities and potential geospatial biases remain underexplored. To address these gaps, we introduce **IMAGEO-Bench**, a benchmark that systematically evaluates LLMs’ image geolocalization abilities. Our key contributions are listed as follows.

- **Comprehensive benchmark datasets.** We compile three datasets with diverse geographic regions, urban/rural scenes, and location indicators, constructed via stratified sampling and augmented with privately collected images to ensure broad coverage.
- **Multi-dimensional evaluation framework.** We propose an evaluation framework that looks beyond standard accuracy to assess spatial precision and computational cost, providing a nuanced understanding of model performance across various dimensions.
- **Geographic bias quantification.** We quantify geographic biases in LLMs by revealing performance disparities across different regions at both global and local scales.
- **Reasoning process analysis.** We employ statistical regression to analyze the reasoning processes behind LLM geolocalization and to identify the most influential visual features.

*Both authors contributed equally to this research, and both are corresponding authors.

2 Related Work

2.1 Image Geolocalization

Image geolocalization in computer vision has focused on two main approaches: classification-based and retrieval-based models [5, 25, 26, 29, 38]. Classification methods (e.g., PlaNet [38]) treat geolocation as a discrete prediction task by assigning an image to a predefined spatial grid. These methods can benefit from global coverage and efficient inference but rely on rigid spatial discretization, which can constrain fine-grained accuracy and interpretability [29]. Retrieval-based methods (e.g., IM2GPS [8]) localize an image by matching it to a geotagged reference set based on visual or semantic similarity. Although enhancements like deep feature learning and probabilistic fusion [35] have improved accuracy, these methods remain reliant on dense reference imagery and struggle in sparsely covered areas. Metric learning models like NetVLAD [1], SAFA [31], and VIGOR [48] further boost retrieval performance using cross-view embeddings and attention mechanisms, particularly effective in visually rich urban settings.

However, these methods often face several limitations: (i) they rely on large labeled datasets and generalize inadequately to unseen or underrepresented regions; (ii) their predictions are often opaque, lacking interpretability or insight into the reasoning process; and (iii) they struggle to incorporate multimodal semantic cues (e.g., textual signage, architectural styles, or cultural markers) that humans intuitively use for geolocation. These limitations call for an approach that can leverage world knowledge and multimodal cues to generalize more effectively. In this regard, LLMs offer a promising solution due to their reasoning abilities, cross-modal integration, and greater interpretability.

2.2 LLMs for Spatial Reasoning

Recent progress in vision-language pre-training has given rise to multimodal LLMs with strong visual reasoning capabilities. Foundation models (e.g., CLIP [27] and ALIGN [14]) have established powerful image-text alignment at web scale, enabling zero-shot classification and retrieval. BLIP-2 [20] further advances this by connecting frozen language models with visual encoders, supporting open-ended visual description and optical character recognition (OCR). Modern multimodal LLMs (e.g., GPT, Gemini, and Qwen) have been demonstrated effective on tasks such as visual question answering [7, 17], document analysis [23], and diagram understanding [11]. However, their spatial reasoning abilities, particularly for fine-grained geolocation, remain underexplored.

A few recent studies have begun to close this gap by evaluating modern foundation models' abilities to localize images [36, 49]. For example, LLMGeo [36] benchmarks GPT-4V and LLaVA on challenging in-the-wild images. It reveals limited accuracy of investigated models and highlights room for improvement. Img2Loc [49] introduces a retrieval-augmented generation (RAG) pipeline that combines vision-language models with large-scale image search to refine coordinate estimates. A more recent study presents a benchmark built on Google Street View images [13], showing that VLMs can achieve sub-300km median errors but suffer from notable failure modes and reasoning transparency.

While these studies represent important progress, they are constrained by task-specific designs, limited geographic scope, and

the absence of standardized evaluation metrics. These underscore the need for a systematic framework to assess LLMs' geolocation capabilities across diverse regions and real-world conditions. To address these gaps, we introduce **IMAGEO-Bench**, a benchmark for systematically evaluating LLMs on location accuracy, computational cost, geographic fairness, and reasoning process based on three newly compiled datasets. The framework of this benchmark is illustrated in Figure 1.

3 Benchmark Dataset Preparation

We construct three benchmark datasets from distinct sources to enable comprehensive evaluation, with their geographic distribution illustrated in Figure 1(a). We opt to build new benchmark datasets for two main reasons. First, this helps mitigate data contamination, as widely used datasets like IM2GPS3k and YFCC4k [8] may have been incorporated in LLM training corpora. Second, our datasets are designed to span diverse visual contexts (e.g., indoor vs. outdoor) and geospatial scales (e.g., global vs. U.S. specific), allowing for a more rigorous assessment of LLM capabilities. Sample images of these benchmark datasets are presented in **Appendix A**. Please note that the distribution of some visual features, namely environment, scene type, and setting, are extracted from the outputs of gemini-2.5-pro, as our objective is not to evaluate the impact of specific image attributes on LLM geolocalization performance, but rather to summarize the model-identified features.

3.1 Dataset-GSS: Global Streetscape Set

Dataset-GSS is derived from the NUS Global Streetscapes dataset [10], a collection of approximately 10 million streetscape images collected from Mapillary and KartaView across 688 cities worldwide. Each image is geo-tagged with precise latitude and longitude coordinates and has city-level labels. Then, the authors of the NUS dataset manually annotate a subset of over 10,000 images with eight contextual attributes: panoramic status, lighting condition, glare, view direction, image quality, reflection, weather, and platform [10].

We build Dataset-GSS by refining this manually labeled subset through a multi-stage filtering process. First, we filter the images with all eight contextual labels, which results in 8,568 images. Second, we only retain the images with the annotations—*quality: good*, *reflection: no*, and *glare: no*—to ensure image quality, narrowing the dataset to 6,178 images. Last, we manually filter to exclude images with insufficient geographic information (e.g., no signs or clear visual cues). After filtering, we obtain Dataset-GSS, which comprises 6,152 high-quality street-level images from 396 cities across 123 countries. This carefully sampled dataset provides a rich variety of scenes captured under diverse geographies, environmental conditions, architectural styles, and cultural contexts. The data distribution of Dataset-GSS is presented in **Appendix B**.

3.2 Dataset-UPC: U.S. POIs Crowdsourced Set

Dataset-UPC is constructed from crowdsourced images from Google Maps Points of Interest (POIs) to capture a diverse range of regions and location types. We first sample POIs from the Google Maps dataset released by UC San Diego [43], which contains 4,963,111 unique POIs across the United States collected up to September 2021. This dataset includes extensive attributes for each POI, including

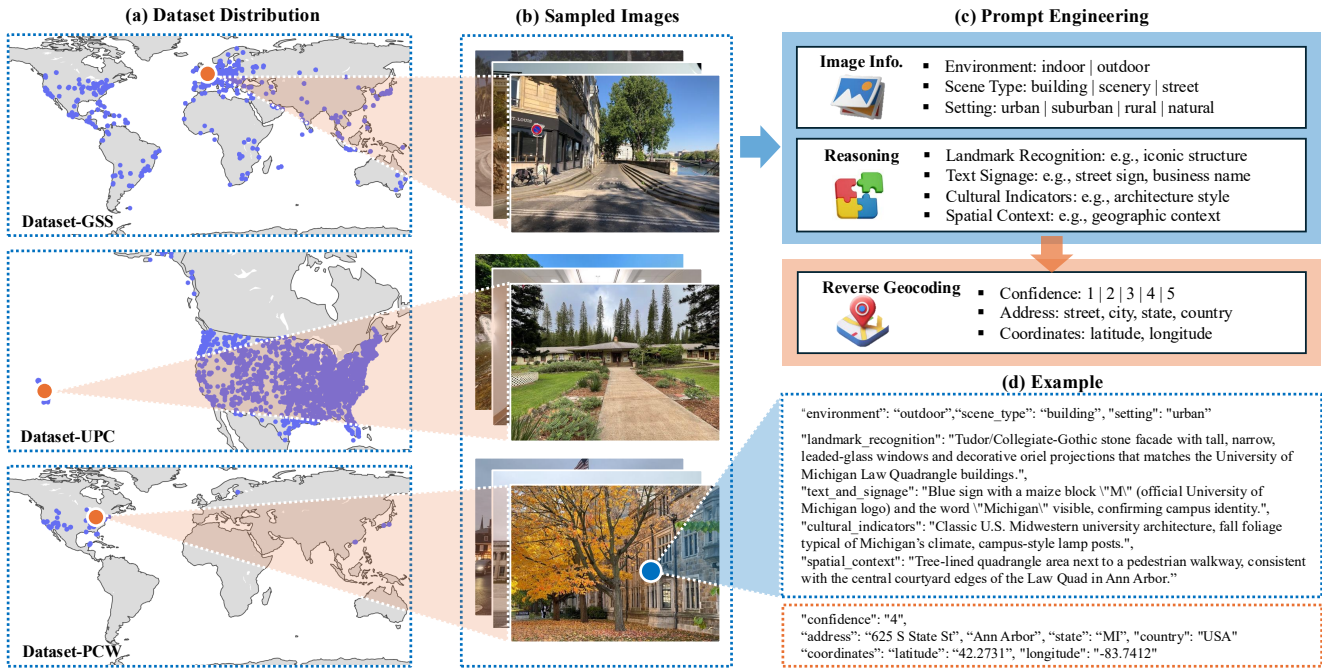


Figure 1: The illustrative framework to implement this study. (a) Data distribution for each benchmark dataset. (b) Sampled images from each dataset. (c) Prompt design. (d) An example of output by the o3 model.

addresses (street, city, state, ZIP code), geolocation coordinates (latitude and longitude), business descriptions, and categorical labels, which makes it ideal for geolocalization evaluation.

To ensure geographic coverage in Dataset-UPC, we employ a multi-stage stratified sampling strategy. We begin with compiling a list of 17 distinct POI categories, including “restaurant,” “hotel,” “park,” and “scenic spot,” to guide the sampling. For each state, we randomly select three POIs from each category, resulting in a pool of 4,325 POIs. We then refine this pool through a two-step filtering process to ensure data usability and integrity. First, we discard entries with non-functional image URLs. Second, we manually remove advertisement images and those containing identifiable human faces. After this curation, Dataset-UPC comprises 2,929 images spanning all 50 states and the District of Columbia.

3.3 Dataset-PCW: Privately Collected Wild Set

Dataset-PCW is constructed as a held-out validation set to prevent potential data leakage. Unlike Datasets-GSS or -UPC, it does not draw from publicly available sources. Instead, it consists of 220 original photo-address pairs collected by the authors. The images span a wide variety of scene types (e.g., natural, rural, urban), weather conditions (e.g., sunny, cloudy, snowy), and temporal contexts (e.g., daytime, nighttime). Since none of the images overlap with existing datasets or known LLM training sources, Dataset-PCW is well suited to evaluate LLMs’ geolocation performance on unseen data.

4 Benchmark Development

IMAGEO-Bench defines a unified end-to-end task for image geolocation. It includes a structured output format, reasoning template,

evaluation metrics, and post-hoc feature-importance analysis tools, allowing for clear and consistent comparisons across LLMs.

4.1 Task Formalization

Given an input image x , the task requires models to predict a structured geographic output tuple: $G = (C, A, (\phi, \lambda))$, where (ϕ, λ) are the predicted latitude and longitude in decimal degrees, A is a structured textual address, and $C \in \{1, 2, 3, 4, 5\}$ denotes the model’s self-reported confidence score. The objective is to minimize the great-circle distance error $d((\phi, \lambda), (\phi^*, \lambda^*))$ between the predicted and ground-truth coordinates. Predictions are provided in a structured JSON format for standardized parsing and evaluation. During inference, models are strictly restricted from accessing external APIs or GPS metadata.

4.2 Output Schema and Reasoning Template

To evaluate LLMs’ geolocalization capabilities, we require models to explicitly reason about the given image by extracting and interpreting salient visual features, as illustrated in Figure 1(c). These features are collected based on prior research identifying layout, signage, text, architecture, road, infrastructure, and buildings as critical cues for image geolocation [13, 22, 33, 40]. Such structured output allows us to systematically analyze models’ reasoning process. Since image geolocalization often depends on recognizing features tied to these specific places, prompting models to surface these elements can facilitate a step-by-step reasoning process similar to that of human geographers. Specifically, the structured model output comprises three key components:

- **Image information:** High-level descriptors characterizing the environment (indoor, outdoor), scene type (building, scenery, street, mixed), and setting (urban, suburban, rural, natural).
- **Reasoning:** A detailed justification for location inference, organized into four distinct categories of visual evidence: (i) Landmark recognition: Unique natural or human-made structures serving as distinctive geographic markers. (ii) Text and signage: Textual clues from visible signs, license plates, storefronts, or other textual indicators. (iii) Cultural indicators: Region-specific architectural styles, cultural symbols, or prevalent societal patterns. (iv) Spatial context: Environmental layout, vegetation patterns, road networks, infrastructure types, or building density.
- **Geolocalization:** The final structured geographic prediction tuple $(C, A, (\phi, \lambda))$, as formally defined before.

4.3 Evaluation Metrics

We establish a set of metrics to measure LLMs’ performance:

- **Identification rate:** It measures the model’s ability to produce a valid output, defined as the percentage of input images for which a complete and correctly formatted JSON is returned. Instances where the model fails to produce a usable output are treated as identification failures.
- **Geographic accuracy:** It evaluates the semantic correctness of the predicted address A_{pred} against the ground truth A_{true} at three administrative levels, including (i) Country accuracy ($Acc_{country}$), (ii) State accuracy (Acc_{state}), and (iii) City accuracy (Acc_{city}). This metric quantifies the proportion of predictions that align with the ground-truth labels.
- **Distance error:** It calculates the great-circle distance d (kilometers) between the predicted coordinates (ϕ_p, λ_p) and the true coordinates (ϕ_t, λ_t) using the Haversine formula:

$$d = 2r \arcsin\left(\sqrt{\sin^2(\Delta\phi/2) + \cos(\phi_p) \cos(\phi_t) \sin^2(\Delta\lambda/2)}\right) \quad (1)$$

where $\Delta\phi = \phi_t - \phi_p$, $\Delta\lambda = \lambda_t - \lambda_p$, and r represents the Earth’s mean radius (6,371 km).

- **Computational cost:** It assesses the model’s efficiency by tracking the computational costs, including the averaged cost Avg_{Cost} and the tokens per inference Avg_{Tokens} (i.e., the average number of input and output tokens consumed for a single image query).

4.4 Post-hoc Feature-Importance Diagnostics

IMAGEO-Bench includes an interpretability module to assess how specific structured output fields correlate with geolocalization performance. This diagnostic suite supports model-agnostic evaluation, identifying which visual attributes are most predictive of successful localization. Specifically, we construct a diagnostic set from each model’s structured JSON outputs. Key categorical predictors—such as environment type, scene category, setting, and landmark presence—are extracted from the predefined schema and one-hot encoded relative to baseline categories. We further define two metrics to represent the geolocation outcome, including (i) a binary indicator representing city-level prediction correctness, and (ii) a continuous log-transformed distance error. Let $\mathbf{x} \in \mathbb{R}^d$ denote this encoded feature vector, and let Y represent the geolocation outcome (e.g., city-level correctness or log-distance error). To quantify feature importance, we fit the following two regression models.

- **Logistic regression.** For the city-level correctness indicator $Y \in \{0, 1\}$, we estimate

$$\mathbb{P}(Y = 1 | \mathbf{x}) = \sigma(\mathbf{w}^\top \mathbf{x} + b), \quad (2)$$

where $\sigma(z) = 1/(1+e^{-z})$ is the sigmoid function. We report $\exp(w_j)$ as the odds ratio of feature j relative to its reference category.

- **Ridge regression.** For the log-distance error, we fit:

$$\log(d) = \mathbf{w}^\top \mathbf{x} + b + \varepsilon, \quad (3)$$

where $\varepsilon \sim \mathcal{N}(0, \sigma^2)$, by minimizing the penalized squared error $\sum_i (y_i - \hat{y}_i)^2 + \lambda \|\mathbf{w}\|_2^2$ with $\lambda = 1.0$.

All predictors are one-hot encoded binary variables, so additional normalization is unnecessary. Because all features share the same scale, the ridge coefficients \mathbf{w} are directly comparable. We aggregate $|w_j|$ within each semantic field to obtain field-level importance.

The importance of the field level is calculated by aggregating the absolute regression coefficients associated with each predictor group. Coefficients are interpreted relative to their baseline categories, with careful consideration given to potential collinearity effects. These diagnostic results provide valuable information on the semantic and visual cues that most strongly influence model geolocalization performance.

5 Experimental Setup

5.1 Prompt Design

We employ a structured prompting methodology to ensure consistent and parsable outputs. Our approach combines a system prompt, which defines the model’s role as a “geocoding analysis” expert, with a main prompt that directs the model to use a step-by-step, chain-of-thought reasoning process. To further guide the model’s inference, we include a one-shot example within the prompt. We mandate that the response be a valid JSON object partitioned into three sections: (i) Image information for high-level scene classification, (ii) reasoning for a detailed analysis of visual evidence, and (iii) image geolocalization for the final coordinate estimation. This standardized design facilitates a direct and objective comparison of the feature extraction and inference capabilities across all models. Specific prompt design is presented in **Appendix C**.

5.2 Model Selection and Experiment Settings

For our benchmark analysis, we select a diverse set of candidate LLMs with vision capabilities from several prominent providers. The models under evaluation include OpenAI’s o3, gpt-4.1, and gpt-4.1-mini; Anthropic’s claude-3.5-haiku; Google’s gemini-1.5-pro, gemini-2.5-flash, and gemini-2.5-pro; and various Llama models, specifically llama-3.2-11b, llama-3.2-90b, and llama-4-maverick-17b. We interface with each model through its designated API.

In our experimental setup, we query each model with a temperature setting of 0.7, which encourages a balance between factual recall and inferential creativity. We log all outputs for each image, including the model’s raw JSON response and error states, to a .jsonl file for subsequent analysis. At the conclusion of each experimental run, we also compute and record a summary of the total operational cost and token consumption. Representative model outputs of image geolocalization are provided in **Appendix H**.

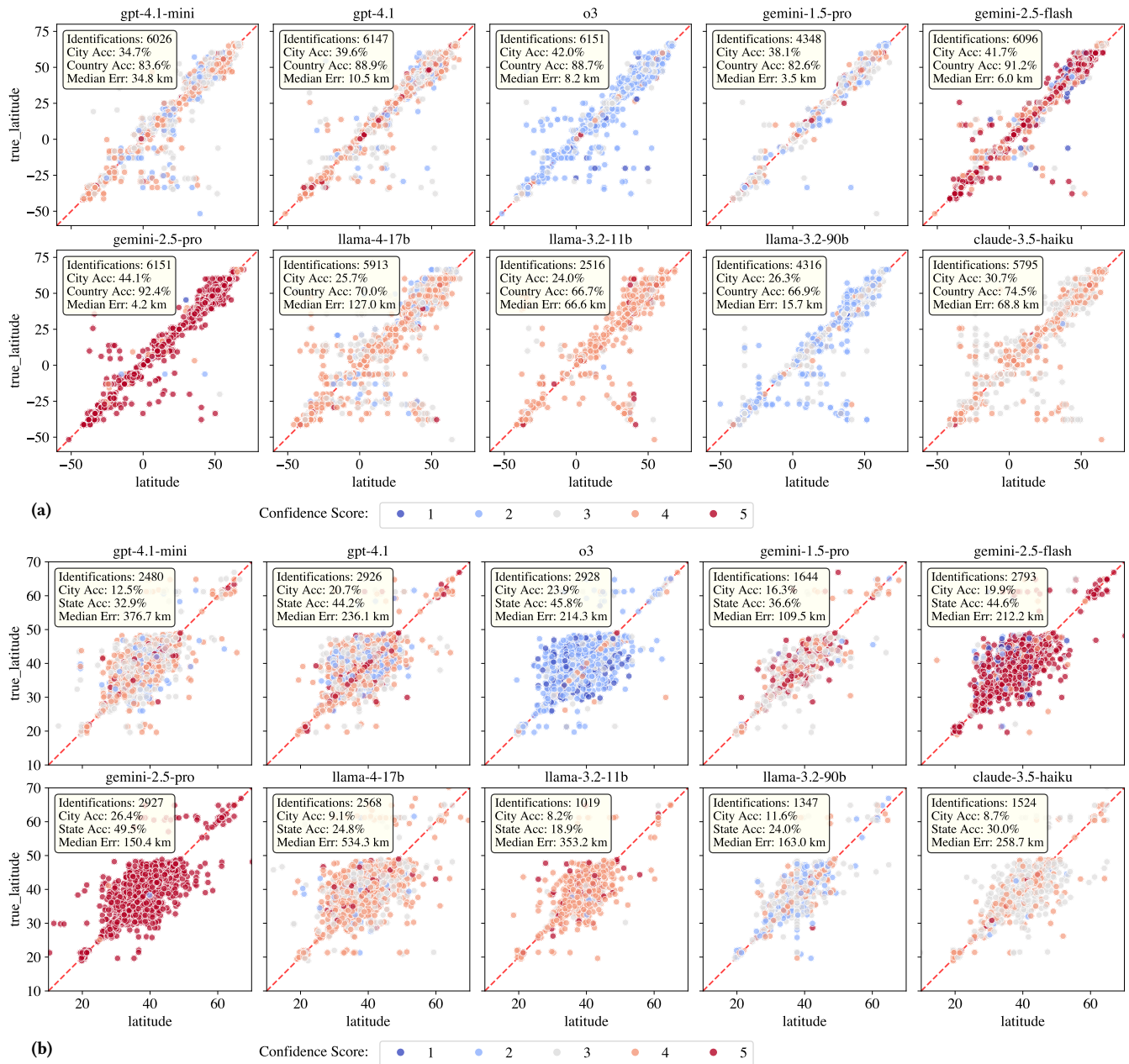


Figure 2: Benchmark performance based on latitude prediction. (a) Dataset-GSS; (b) Dataset-UPC. Perfect predictions lie on the red dashed diagonal line. The proximity of points to this line indicates the model’s accuracy, with the color of each point representing the model’s self-reported confidence score on a scale of 1 to 5.

6 Results and Analysis

6.1 Benchmark Performance

To benchmark LLMs’ performance, we generate two sets of scatter plots using the introduced metrics. Table 1 presents a quantitative summary, including accuracy at various geospatial scales, median distance error, and computational costs. For visual analysis, Figure 2 displays scatter plots for latitude prediction on (a) Dataset-GSS and (b) Dataset-UPC, while corresponding longitude results are

provided in Appendix D. The benchmark performance for Dataset-PCW is included in Appendix E.

Performance across Dataset-GSS and Dataset-UPC shows clear differences, with most LLMs exhibiting higher prediction accuracy on Dataset-GSS. This discrepancy is likely due to the inherent characteristics of the compiled datasets. Dataset-GSS primarily consists of publicly available global street-level images captured in outdoor environments, which provide clear geographic indicators. In contrast, Dataset-UPC comprises crowdsourced images contributed by

Table 1: LLM performance benchmark based on Dataset-GSS and Dataset-UPC.

Model	Dataset-GSS					Dataset-UPC						
	City Acc (%)	Country Acc (%)	Mean Dist (km)	Median Dist (km)	Avg Tokens	Avg Cost (\$)	City Acc (%)	State Acc (%)	Mean Dist (km)	Median Dist (km)	Avg Tokens	Avg Cost (\$)
gpt-4.1-mini	34.7%	83.6%	381.1	34.8	3245	0.00164	12.5%	32.9%	768.8	376.7	1496	0.00092
gpt-4.1	39.6%	88.9%	296.1	10.5	1842	0.00536	20.7%	44.2%	685.8	236.1	1465	0.00455
o3	42.0%	88.7%	288.1	8.2	2912	0.01460	23.9%	45.8%	662.7	214.3	2281	0.01150
gemini-1.5-pro	38.1%	82.6%	161.4	3.5	1178	0.00243	16.3%	36.6%	406.5	109.5	1165	0.00237
gemini-2.5-flash	41.7%	91.2%	227.0	6.0	1379	0.00141	19.9%	44.6%	587.7	212.2	1326	0.00128
gemini-2.5-pro	44.1%	92.4%	216.3	4.2	1367	0.00556	26.4%	49.5%	544.4	150.4	1328	0.00517
llama-4-17b	25.7%	70.0%	840.3	127.0	2961	0.00093	9.1%	24.8%	1217.5	534.3	1767	0.00061
llama-3.2-11b	24.0%	66.7%	797.4	66.6	823	0.00015	8.2%	18.9%	955.5	353.2	822	0.00015
llama-3.2-90b	26.3%	66.9%	382.9	15.7	7211	0.00865	11.6%	24.0%	706.8	163.0	5206	0.00625
claude-3.5-haiku	30.7%	74.5%	568.2	68.8	2478	0.00281	8.7%	30.0%	697.1	258.7	1421	0.00190

Google Maps users, many of which are taken indoors, lack explicit geographic cues or distinctive architectural details. These characteristics significantly complicate accurate identification of geolocation. As a result, most LLMs achieve higher accuracy with Dataset-GSS across all evaluated levels, including city, country, and state, and report lower median distance errors.

Closed-source models consistently outperform their open-source counterparts across both datasets. Specifically, gemini-2.5-pro achieves remarkable results in Dataset-GSS, with a median error of 4.2 km and country-level accuracy of 92.4%. Other top performers like gpt-4.1 and o3 maintain high performance with median errors of 10.5 km and 8.2 km, respectively, in Dataset-GSS. Conversely, open-source models such as llama-4-17b and llama-3.2-11b exhibit substantially higher median errors (e.g., 127.0 km for llama-4-17b in Dataset-GSS and 534.3 km in Dataset-UPC). This performance gap likely originates from proprietary advantages of closed-source providers, including larger training datasets, richer geospatial corpora, and more refined model architectures.

We also observe a clear scaling trend, where larger models generally exhibit stronger capabilities. For example, gpt-4.1 surpasses its smaller counterpart, gpt-4.1-mini, with a city-level accuracy of 39.6% versus 34.7% and a much lower median distance error (10.5 km versus 34.8 km). Similarly, llama-3.2-90b improves upon llama-3.2-11b with a city-level accuracy of 26.3% versus 24.0%, and a median distance error of 15.7 km versus 66.6 km. However, performance differences are not solely size-dependent. Smaller models like gemini-2.5-flash (city accuracy 41.7%, median error 6.0 km) outperform many larger models, suggesting that other factors (e.g., model architecture, multimodal fusion techniques, and training quality) can contribute to improved performance. This reinforces that scaling is helpful but not sufficient on its own.

Confidence scores vary significantly across the models, among which gemini-2.5-pro exhibits the highest confidence, while o3 reports the lowest. Even within a single provider, confidence levels differ: for instance, gpt-4.1 is substantially more confident than gpt-4.1-mini, and gemini-2.5-pro scores higher than gemini-1.5-pro. For models like gpt-4.1, o3, and claude-3.5-haiku, higher confidence scores generally align with better prediction accuracy within the same model. However, higher confidence does not always imply greater performance across models. For instance, gemini-2.5-pro shows a higher confidence distribution than o3, yet their performance in Dataset-GSS is comparable (median errors of 4.2 km

versus 8.2 km). These findings indicate that confidence alone is not a reliable proxy for model accuracy and should be interpreted in conjunction with performance metrics.

In addition, the computational cost reveal significant variations across models. llama-3.2-11b emerges as the most efficient option, using only ~823 tokens at \$0.00015 per request, while o3 is the most expensive model at \$0.01460 per request in Dataset-GSS. However, this cost savings of open-sourced models comes with substantially lower performance. Among closed-source models, gemini-2.5-flash offers an optimal balance, achieving 41.7% city accuracy at just \$0.00141 per request. Interestingly, model size doesn't always correlate to resource consumption. For example, gpt-4.1-mini consumes 3,245 tokens despite its "mini" label, nearly 3× of gemini-1.5-pro's 1,178 tokens. These findings highlight a trade-off between cost-efficiency and performance for effective image geolocalization.

6.2 Geospatial Analysis

We conduct geospatial analyses on Dataset-GSS and Dataset-UPC to evaluate model performance across geographic regions and scales. In Dataset-GSS (Figure 3), we calculate country-level accuracy for nations with over 20 samples to ensure statistical reliability. Results reveal pronounced geographic bias and model variability. Models such as o3 and gemini-2.5-pro achieve near-perfect accuracy (approaching 1.0) in regions like North America, Russia, and Australia. In contrast, llama-3.2-11b consistently underperforms, with accuracy often below 0.6 and approaching zero in several Latin European countries. Models like llama-3.2-90b and claude-3.5-haiku show intermediate accuracy (0.6–0.9). It is noting that the United States, Australia, and West European Countries maintain high accuracy across all models, suggesting strong model generalization in these well-represented regions.

In Dataset-UPC (Figure 4), we again observe distinct geographic disparities in model performance across U.S. states. Specifically, gemini-2.5-flash, gemini-2.5-pro, and o3 consistently perform well, particularly in California, Hawaii, and Florida. In contrast, llama-3.2-11b falls below 0.5 accuracy in nearly all states. gpt-4.1 shows moderate performance, with accuracy typically between 0.6 and 0.8 in coastal regions. California and Florida emerge as consistent high-performing states across models, likely due to their dense urban environments and distinctive landmarks that can facilitate image geolocalization.

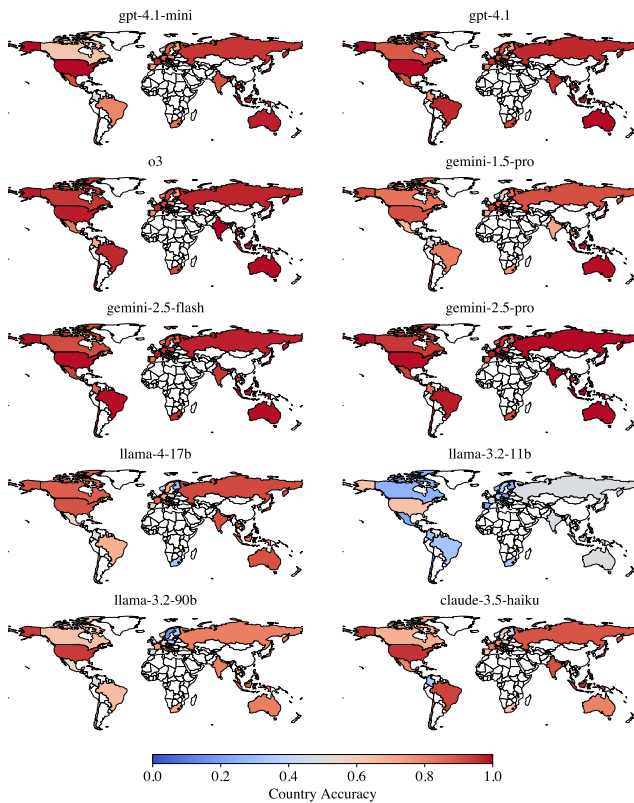


Figure 3: Country-level averaged accuracy across models on Dataset-GSS (a threshold of 20 sampled images).

Together, the results from both datasets illustrate potential geospatial biases in model behavior. High performance in regions like the United States, Australia, and parts of Western Europe points to the models’ strong alignment with densely sampled, visually distinctive, and data-rich environments. In contrast, accuracy declines sharply in countries and states with fewer training representations or more ambiguous visual features. These patterns reflect a potential limitation that LLMs are not yet equipped to generalize robustly across diverse global geographies.

6.3 Reasoning Analysis

6.3.1 *Feature attribution via reasoning.* We apply logistic regression diagnostics to examine the features for the LLM reasoning process. The summarized result for Dataset-GSS is illustrated in Figure 5. Image elements are categorized into four semantic groups: environment, scene type, setting, and landmark. Across the evaluated LLMs, we observe consistent trends as well as model-specific variations. The main findings are as follows.

First, nearly all models strongly favor urban and outdoor environments while consistently penalizing rural, natural, and indoor scenes. One possible explanation is that dense urban contexts, featuring detailed façades, prominent signage, and infrastructure elements (e.g., roads and street furniture), provide reliable visual cues for accurate geolocalization. Conversely, natural scenes, which often lack distinctive visual anchors, pose significant localization challenges, as reflected by consistently negative model associations.

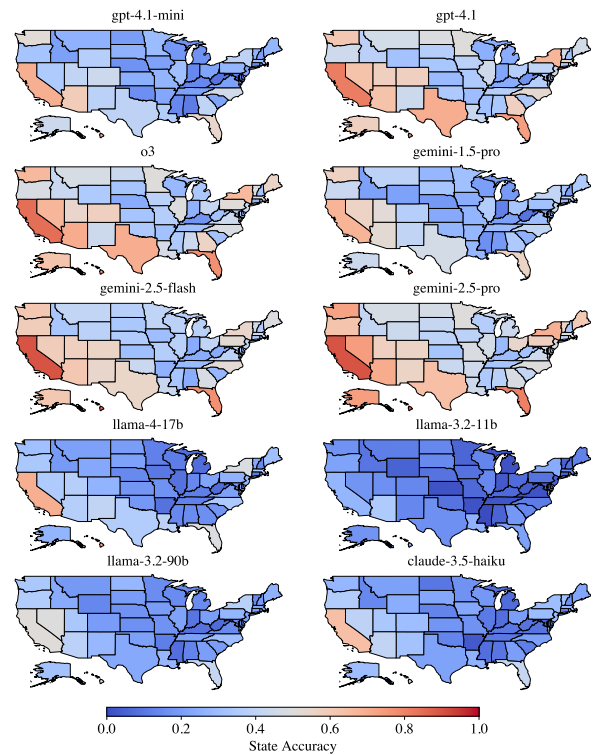


Figure 4: U.S. state-level averaged accuracy across models on Dataset-UPC (a threshold of 20 sampled images).

Second, regarding scene type, street-level imagery tends to provide stronger localization signals than building façades or general scenery. This is likely because street scenes often contain rich contextual cues (e.g., textual signage, road markings, and distinctive urban infrastructure) that are both visually salient and semantically interpretable by LLMs. In contrast, scenic images without clear architectural landmarks can negatively impact prediction accuracy.

Third, the presence of distinctive landmarks consistently improves the geolocation performance across nearly all models. Landmark cues are typically assigned strong positive weights, indicating their critical role in guiding correct predictions. However, the claude-3.5-haiku model is a notable outlier: it assigns marginal or even negative weights to the landmark cue. A post-hoc audit reveals that it labels “landmark = yes” on 99.67% of images, compared to 41.77% for all other models. This over-identification of landmarks suggests that the model frequently misclassifies ordinary structures as distinctive, thereby diluting the predictive value of this feature.

Overall, current LLMs perform best when presented with clear, distinct visual elements, including textual signage, iconic architecture, and densely structured urban layouts. They struggle significantly, however, in contexts that lack easily verbalizable landmarks or signage. Additional analyses and visualizations, including distance error evaluations and results on the UPC and PCW datasets, are provided in **Appendix F**.

6.3.2 *Word-Cloud Analysis.* In addition, we perform a word cloud analysis to provide a lexical overview of the cues used by the o3 model in three datasets, as shown in Figure 6. First, the terms of the traffic infrastructure dominate the model outputs. Terms such

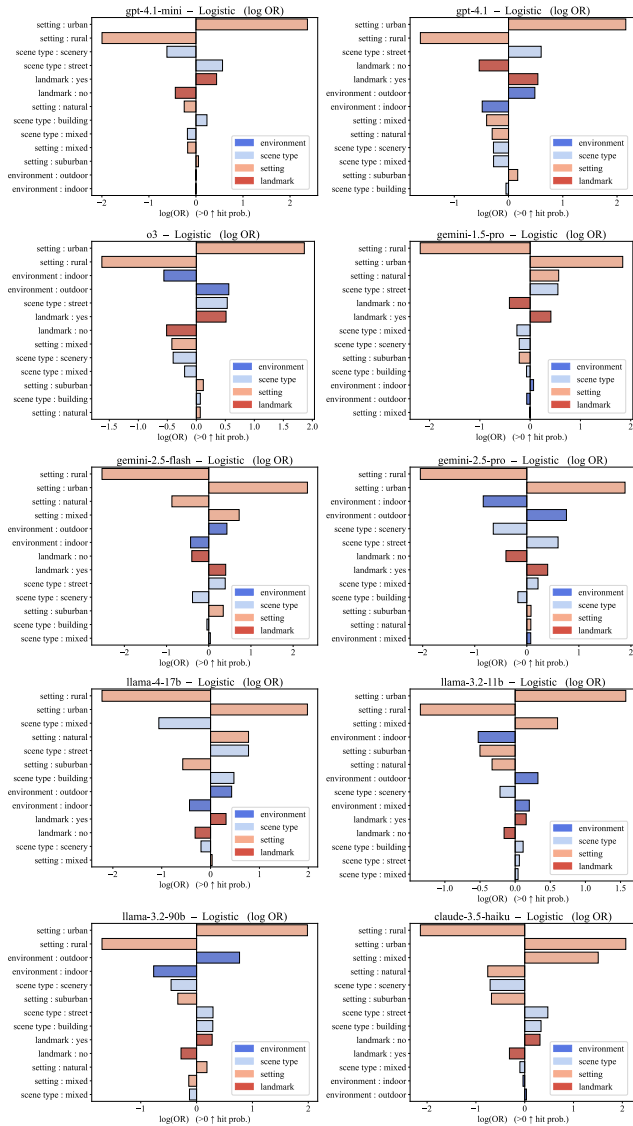


Figure 5: Log-odds coefficients from diagnostic logistic regression on Dataset-GSS. Positive values increase the likelihood of correct city prediction; negative values decrease it.

as “sign,” “street,” “road,” “lane,” and “traffic light” appear more frequently, reflecting the strong reliance on OCR-visible elements and road geometry. Second, color terms, such as “red,” “white,” “yellow,” “blue,” “green,” function as indirect geographic signals. These cues are often tied to traffic regulations (e.g., yellow center lines in the United States vs. white in Europe), enabling the model to infer regional priors based on color patterns. Third, regional adjectives are sparse but informative. Although generic terms like “brick” or “trees” are common, less frequent modifiers such as “German,” “Japanese,” or “American” suggest that o3 rarely states a location outright, instead embedding regional cues in compound phrases like “license plates” or “right hand” (driving side). In general, the lexical profile indicates that o3 is highly based on discrete, regulative, and text-based anchors, while underutilizing cues related to



Figure 6: Mixed unigram-bigram word cloud derived from the reasoning fields of the o3 model. Font size reflects token frequency.

vegetation, climate, or terrain. A broader comparison across nine additional models is provided in Appendix G.

7 Discussion and Conclusions

Our study introduces **IMAGEO-Bench**, a comprehensive benchmark designed to evaluate the image geolocation capabilities of LLMs across accuracy, computational cost, geographic fairness, and reasoning process. Our key findings are summarized below.

Closed-source models lead in performance but at a higher cost. Models like gemini-2.5-pro and o3 consistently outperform open-source alternatives in accuracy and distance error. However, this comes with significantly higher computational costs. gemini-2.5-flash offers a compelling balance between cost-efficiency and accuracy. This suggests that model architecture, training data quality, and modality alignment can outweigh parameter count in determining performance.

Geographic performance disparities reflect potential training data and reasoning biases. Models consistently perform better in high-resource, visually distinctive regions like North America, Western Europe, and Australia, while struggling in underrepresented or ambiguous areas. States like California and Florida see higher accuracy, likely due to richer training data and clearer visual cues. These disparities highlight limitations in global generalization and raise concerns about geographic fairness.

Models rely on visual anchors, not holistic understanding. LLMs tend to perform better in outdoor urban scenes with clear cues like signage and landmarks, while rural, natural, and indoor images lead to higher errors due to limited identifiable features. Models can infer broad regional context (e.g., country-level), but struggle with fine-grained localization in the absence of strong visual anchors. Moreover, spatial layout or image composition appears to have little impact on prediction performance.

This study opens several avenues for future research. One direction could conduct a more comprehensive study covering diverse geographies and scene types to assess model generalization under real-world variability. Another future work could explore how language-based cues contribute to geolocation predictions, especially in scenes lacking visual anchors. Lastly, future work could explore strategies such as data augmentation or region-adaptive prompting to reduce geographic bias—an essential step toward building more equitable and globally robust geolocation systems.

References

- [1] Relja Arandjelović, Petr Gronat, Akihiko Torii, Tomáš Pajdla, and Josef Sivic. 2016. NetVLAD: CNN Architecture for Weakly Supervised Place Recognition. In *Proc. IEEE Conf. on Computer Vision and Pattern Recognition (CVPR)*. 5297–5307. <https://doi.org/10.1109/CVPR.2016.572>
- [2] Jan Brejcha and Martin Čadik. 2017. State-of-the-art in visual geo-localization. *Pattern Analysis and Applications* 20, 3 (2017), 613–637.
- [3] Tom Brown, Benjamin Mann, Nick Ryder, Melanie Subbiah, Jared D Kaplan, Prafulla Dhariwal, Arvind Neelakantan, Pranav Shyam, Girish Sastry, Amanda Askell, et al. 2020. Language models are few-shot learners. *Advances in neural information processing systems* 33 (2020), 1877–1901.
- [4] Boyuan Chen, Zhuo Xu, Sean Kirmani, Brain Ichter, Dorsa Sadigh, Leonidas Guibas, and Fei Xia. 2024. Spatialvlm: Endowing vision-language models with spatial reasoning capabilities. In *Proceedings of the IEEE/CVF Conference on Computer Vision and Pattern Recognition*. 14455–14465.
- [5] Brandon Clark, Alec Kerrigan, Parth Parag Kulkarni, Vicente Vivanco Cepeda, and Mubarak Shah. 2023. Where we are and what we're looking at: Query based worldwide image geo-localization using hierarchies and scenes. In *Proceedings of the IEEE/CVF Conference on Computer Vision and Pattern Recognition*. 23182–23190.
- [6] Lizhou Fan, Wenyue Hua, Xiang Li, Kaijie Zhu, Mingyu Jin, Lingyao Li, Haoyang Ling, Jinkui Chi, Jindong Wang, Xin Ma, et al. 2024. Nphardeval4v: A dynamic reasoning benchmark of multimodal large language models. *arXiv preprint arXiv:2403.01777* (2024).
- [7] Jiaxian Guo, Junnan Li, Dongxu Li, Anthony Meng Huat Tiong, Boyang Li, Dacheng Tao, and Steven Hoi. 2023. From images to textual prompts: Zero-shot visual question answering with frozen large language models. In *Proceedings of the IEEE/CVF conference on computer vision and pattern recognition*. 10867–10877.
- [8] James Hays and Alexei A Efros. 2008. IM2GPS: estimating geographic information from a single image. In *2008 IEEE Conference on Computer Vision and Pattern Recognition*. IEEE, 1–8. <https://doi.org/10.1109/CVPR.2008.4587784>
- [9] James Hays and Alexei A Efros. 2014. Large-scale image geolocation. In *Multimodal location estimation of videos and images*. Springer, 41–62.
- [10] Yujun Hou, Matias Quintana, Maxim Khomiakov, Winston Yap, Jiani Ouyang, Koichi Ito, Zeyu Wang, Tianhong Zhao, and Filip Biljecki. 2024. Global Streetscapes—A comprehensive dataset of 10 million street-level images across 688 cities for urban science and analytics. *ISPRS Journal of Photogrammetry and Remote Sensing* 215 (2024), 216–238.
- [11] Anwen Hu, Yaya Shi, Haiyang Xu, Jiabo Ye, Qinghao Ye, Ming Yan, Chenliang Li, Qi Qian, Ji Zhang, and Fei Huang. 2024. mplug-paperowl: Scientific diagram analysis with the multimodal large language model. In *Proceedings of the 32nd ACM International Conference on Multimedia*. 6929–6938.
- [12] Wenyue Hua, Kaijie Zhu, Lingyao Li, Lizhou Fan, Shuhang Lin, Mingyu Jin, Haochen Xue, Zelong Li, Jindong Wang, and Yongfeng Zhang. 2024. Disentangling logic: The role of context in large language model reasoning capabilities. *arXiv preprint arXiv:2406.02787* (2024).
- [13] Neel Jay, Hieu Minh Nguyen, Trung Dung Hoang, and Jacob Haimès. 2025. Evaluating precise geolocation inference capabilities of vision language models. *arXiv preprint arXiv:2502.14412* (2025).
- [14] Chao Jia, Yinfei Yang, Ye Xia, Yi-Ting Chen, Zarana Parekh, Hieu Pham, Quoc Le, Yunhsuan Sung, Zhen Li, and Tom Duerig. 2021. Scaling Up Visual and Vision-Language Representation Learning with Noisy Text Supervision. In *Proc. Int. Conf. on Machine Learning (ICML)*. 4904–4916.
- [15] Hyo Jin Kim, Enrique Dunn, and Jan-Michael Frahm. 2017. Learned contextual feature reweighting for image geo-localization. In *Proceedings of the IEEE Conference on Computer Vision and Pattern Recognition*. 2136–2145.
- [16] VijayaKumar Kadha, Sambit Bakshi, and Santos Kumar Das. 2025. Unravelling Digital Forgeries: A Systematic Survey on Image Manipulation Detection and Localization. *Comput. Surveys* 57, 12 (2025), 1–36.
- [17] Jiayi Kuang, Ying Shen, Jingyou Xie, Hao hao Luo, Zhe Xu, Ronghao Li, Yinghui Li, Xianfeng Cheng, Xika Lin, and Yu Han. 2025. Natural language understanding and inference with mllm in visual question answering: A survey. *Comput. Surveys* 57, 8 (2025), 1–36.
- [18] Alexandre Lacoste, Nils Lehmann, Pau Rodriguez, Evan Sherwin, Hannah Kerner, Björn Lütjens, Jeremy Irvin, David Dao, Hamed Alemohammad, Alexandre Drouin, et al. 2023. Geo-bench: Toward foundation models for earth monitoring. *Advances in Neural Information Processing Systems* 36 (2023), 51080–51093.
- [19] Hao Li, Fabian Deuser, Wenping Yin, Xuanshu Luo, Paul Walther, Gengchen Mai, Wei Huang, and Martin Werner. 2025. Cross-view geolocation and disaster mapping with street-view and VHR satellite imagery: A case study of Hurricane IAN. *ISPRS Journal of Photogrammetry and Remote Sensing* 220 (2025), 841–854.
- [20] Junnan Li, Dongxu Li, Silvio Savarese, and Steven Hoi. 2023. BLIP-2: Bootstrapping Language-Image Pre-training with Frozen Image Encoders and Large Language Models. In *Proc. 40th Int. Conf. on Machine Learning (ICML)*, Vol. 202. PMLR, 19730–19742.
- [21] Lingyao Li, Dawei Li, Zhenhui Ou, Xiaoran Xu, Jingxiao Liu, Zihui Ma, Runlong Yu, and Min Deng. 2025. LLMs as World Models: Data-Driven and Human-Centered Pre-Event Simulation for Disaster Impact Assessment. *arXiv preprint arXiv:2506.06355* (2025).
- [22] Ling Li, Yao Zhou, Yuxuan Liang, Fugee Tsung, and Jiaheng Wei. 2025. Recognition through Reasoning: Reinforcing Image Geo-localization with Large Vision-Language Models. *arXiv preprint arXiv:2506.14674* (2025).
- [23] Xin Li, Yunfei Wu, Xinghua Jiang, Zhihao Guo, Mingming Gong, Haoyu Cao, Yinsong Liu, Deqiang Jiang, and Xing Sun. 2024. Enhancing visual document understanding with contrastive learning in large visual-language models. In *Proceedings of the IEEE/CVF Conference on Computer Vision and Pattern Recognition*. 15546–15555.
- [24] Tsung-Yi Lin, Serge Belongie, and James Hays. 2013. Cross-view image geolocation. In *Proceedings of the IEEE Conference on Computer Vision and Pattern Recognition*. 891–898.
- [25] Eric Muller-Budack, Kader Pustu-Iren, and Ralph Ewerth. 2018. Geolocation estimation of photos using a hierarchical model and scene classification. In *Proceedings of the European conference on computer vision (ECCV)*. 563–579.
- [26] Shraman Pramanick, Ewa M Nowara, Joshua Gleason, Carlos D Castillo, and Rama Chellappa. 2022. Where in the world is this image? transformer-based geo-localization in the wild. In *European Conference on Computer Vision*. Springer, 196–215.
- [27] Alec Radford, Jong Wook Kim, and Christopher et al. Hallacy. 2021. Learning Transferable Visual Models from Natural Language Supervision. In *Proc. Int. Conf. on Machine Learning (ICML)*. 8748–8763.
- [28] Noe Samano, Mengjie Zhou, and Andrew Calway. 2020. You are here: Geolocation by embedding maps and images. In *European Conference on Computer Vision*. Springer, 502–518.
- [29] Paul Hongsuck Seo, Tobias Weyand, Jack Sim, and Bohyung Han. 2018. Cplanet: Enhancing image geolocation by combinatorial partitioning of maps. In *Proceedings of the European Conference on Computer Vision (ECCV)*. 536–551.
- [30] David G Shatwell, Ishan Rajendrakumar Dave, Sirmam Swetha, and Mubarak Shah. 2025. GT-Loc: Unifying When and Where in Images Through a Joint Embedding Space. *arXiv preprint arXiv:2507.10473* (2025).
- [31] Zhicheng Shi, Yang Li, Siyu Li, and Jiebo Luo. 2020. SAFA: Structure-Aware Feature Aggregation for Cross-View Image-Based Geo-Localization. In *Proc. ACM Int. Conf. on Multimedia (MM)*. 1633–1641. <https://doi.org/10.1145/3394171.3413569>
- [32] Kexin Tian, Jingrui Mao, Yunlong Zhang, Jiwan Jiang, Yang Zhou, and Zhengzhong Tu. 2025. Nuscenes-spatialqa: A spatial understanding and reasoning benchmark for vision-language models in autonomous driving. *arXiv preprint arXiv:2504.03164* (2025).
- [33] Yicong Tian, Chen Chen, and Mubarak Shah. 2017. Cross-view image matching for geo-localization in urban environments. In *Proceedings of the IEEE Conference on Computer Vision and Pattern Recognition*. 3608–3616.
- [34] Vicente Vivanco Cepeda, Gaurav Kumar Nayak, and Mubarak Shah. 2023. Geo-CLIP: Clip-Inspired Alignment between Locations and Images for Effective Worldwide Geo-localization. In *Advances in Neural Information Processing Systems (NeurIPS)*.
- [35] Nam Vo and David W. Jacobs. 2017. Revisiting IM2GPS in the Deep Learning Era. *arXiv preprint arXiv:1705.04838* (2017).
- [36] Zhiqiang Wang, Dejia Xu, Rana Muhammad Shahroz Khan, Yanbin Lin, Zhiwen Fan, and Xingquan Zhu. 2024. lmgeo: Benchmarking large language models on image geolocation in-the-wild. *arXiv preprint arXiv:2405.20363* (2024).
- [37] Jason Wei, Xuezhi Wang, Dale Schuurmans, Maarten Bosma, Fei Xia, Ed Chi, Quoc V Le, Denny Zhou, et al. 2022. Chain-of-thought prompting elicits reasoning in large language models. *Advances in neural information processing systems* 35 (2022), 24824–24837.
- [38] Tobias Weyand, Ilya Kostrikov, and James Philbin. 2016. PlaNet - Photo Geolocation with Convolutional Neural Networks. In *European Conference on Computer Vision (ECCV)*. Springer, 37–55. https://doi.org/10.1007/978-3-319-46484-8_3
- [39] Scott Workman, Richard Souvenir, and Nathan Jacobs. 2015. Wide-area image geolocation with aerial reference imagery. In *Proceedings of the IEEE International Conference on Computer Vision*. 3961–3969.
- [40] Meiliu Wu and Qunying Huang. 2022. Im2city: image geo-localization via multimodal learning. In *Proceedings of the 5th ACM SIGSPATIAL International Workshop on AI for Geographic Knowledge Discovery*. 50–61.
- [41] Wenshan Wu, Shaoguang Mao, Yadong Zhang, Yan Xia, Li Dong, Lei Cui, and Furu Wei. 2024. Mind's eye of LLMs: visualization-of-thought elicits spatial reasoning in large language models. *Advances in Neural Information Processing Systems* 37 (2024), 90277–90317.
- [42] Shixiong Xu, Chenghao Zhang, Lubin Fan, Gaofeng Meng, Shiming Xiang, and Jieping Ye. 2024. Addressclip: Empowering vision-language models for city-wide image address localization. In *European Conference on Computer Vision*. Springer, 76–92.
- [43] An Yan, Zhankui He, Jiacheng Li, Tianyang Zhang, and Julian McAuley. 2023. Personalized showcases: Generating multi-modal explanations for recommendations. In *Proceedings of the 46th International ACM SIGIR Conference on Research*

and *Development in Information Retrieval*. 2251–2255.

- [44] Jihan Yang, Shusheng Yang, Anjali W Gupta, Rilyn Han, Li Fei-Fei, and Saining Xie. 2025. Thinking in space: How multimodal large language models see, remember, and recall spaces. In *Proceedings of the Computer Vision and Pattern Recognition Conference*. 10632–10643.
- [45] Qiang Yi and Lianlei Shan. 2025. Geolocsft: Efficient visual geolocation via supervised fine-tuning of multimodal foundation models. *arXiv preprint arXiv:2506.01277* (2025).
- [46] Wenping Yin, Yong Xue, Ziqi Liu, Hao Li, and Martin Werner. 2025. LLM-enhanced disaster geolocalization using implicit geoinformation from multimodal data: A case study of Hurricane Harvey. *International Journal of Applied Earth Observation and Geoinformation* 137 (2025), 104423.
- [47] Amir Roshan Zamir and Mubarak Shah. 2014. Image geo-localization based on multiplexed neighbor feature matching using generalized graphs. *IEEE transactions on pattern analysis and machine intelligence* 36, 8 (2014), 1546–1558.
- [48] Yanhua Zhong, Yuqiang Wu, Sheng Zheng, Yi Yang, and Zhiwu Ma. 2021. VIGOR: Cross-View Image Geo-Localization Beyond One-to-One Retrieval. In *Proc. IEEE/CVF Conf. on Computer Vision and Pattern Recognition (CVPR)*. 8636–8645. <https://doi.org/10.1109/CVPR46437.2021.00853>
- [49] Zhongliang Zhou, Jieli Zhang, Zihan Guan, Mengxuan Hu, Ni Lao, Lan Mu, Sheng Li, and Gengchen Mai. 2024. Img2Loc: Revisiting image geolocalization using multi-modality foundation models and image-based retrieval-augmented generation. In *Proceedings of the 47th international acm sigir conference on research and development in information retrieval*. 2749–2754.
- [50] Sijie Zhu, Mubarak Shah, and Chen Chen. 2022. Transgeo: Transformer is all you need for cross-view image geo-localization. In *Proceedings of the IEEE/CVF Conference on Computer Vision and Pattern Recognition*. 1162–1171.

A Sample Images from Benchmark Datasets

Sample images from our three datasets in the benchmark are presented in Figure 7.

B Data Distribution from Benchmark Datasets

The sample distribution based on annotated features provided by the NUS team [10] for Dataset-GSS is shown in Table 2. Table 3 presents the distribution of features extracted from model outputs by gemini-2.5-pro across our benchmark datasets. Please note that these features are not human-annotated, as our goal is not to evaluate the influence of specific image attributes on LLMs’ geolocalization performance.

Table 2: Sample distribution of Dataset-GSS.

Feature	Value	Count
lighting_condition	day	5601
lighting_condition	dusk/dawn	319
lighting_condition	night	232
view_direction	front/back	5451
view_direction	side	701
weather	clear	4638
weather	cloudy	1189
weather	snowy	175
weather	rainy	147
weather	foggy	3

C Prompt Design

The prompt design shown below (Figure 8) enables LLMs to perform image geolocalization from a given image. The prompt design shown below is guided by two key strategies: (i) chain-of-thought reasoning [37] and (ii) few-shot learner guidance [3]. Each model is instructed to follow a structured reasoning process: first, analyze the visual content (e.g., landmarks, textual signage, and cultural

Table 3: Sample distribution in datasets based on gemini-pro-2.5.

Feature	Value	GSS	UPC	PCW
environment	outdoor	6144	2400	264
	indoor	2	522	4
	mixed	5	5	2
scene_type	street	4636	120	33
	mixed	1072	685	141
	scenery	414	403	56
	building	29	1719	40
setting	urban	4350	595	149
	suburban	998	1675	81
	rural	755	373	8
	natural	48	283	31
	mixed	0	1	1

indicators); then, apply chain-of-thought reasoning to integrate these observations; and finally, produce geocoded predictions accompanied by confidence scores.

D Longitude Analysis on Datasets-GSS & -UPC

Figure 9 presents model performance on longitude prediction, complementing our earlier analysis of latitude. Overall trends are consistent: closed-source models generally achieve higher accuracy, while open-source models exhibit greater variance. In Dataset-GSS (Figure 9(a)), most models produce predictions that align well with the ground-truth longitudes, as evidenced by tight clustering along the diagonal. Closed-source models such as gemini-2.5-pro, o3, and gpt-4.1 demonstrate strong alignment, whereas open-source models show more scattered predictions across the longitude range.

Despite the similarity with latitude analysis (Figure 2, the longitude scatter plots reveal clear differences. For Dataset-UPC (Figure 9(b)), predictions form a distinctive cube-like shape: both predicted (x-axis) and true (y-axis) longitudes fall between approximately -120° and -66° , consistent with the full longitudinal extent of the U.S. continent. However, rather than aligning along the diagonal, predictions are densely concentrated in the middle of this range. This pattern is observed across most models, regardless of architecture or source. This pattern further suggests that, in the absence of clear visual cues, models often default to generic or centrally located longitude values. While such predictions typically fall within plausible U.S. bounds, they are frequently assigned to widely dispersed ground-truth locations. A likely explanation is that, unlike latitude—which can be inferred from environmental features such as vegetation, climate, or sun angle—longitude provides fewer visually distinctive signals across many U.S. scenes. Consequently, even high-performing models tend to produce centralized, non-specific longitude estimates when visual evidence is ambiguous.

E Benchmark Performance on Dataset-PCW

Table 4 shows the performance of models’ geolocation prediction on unseen images from Dataset-PWC. The results reveal similar performance trends across models as observed with the other two datasets (see Table 1), with closed-source models maintaining an

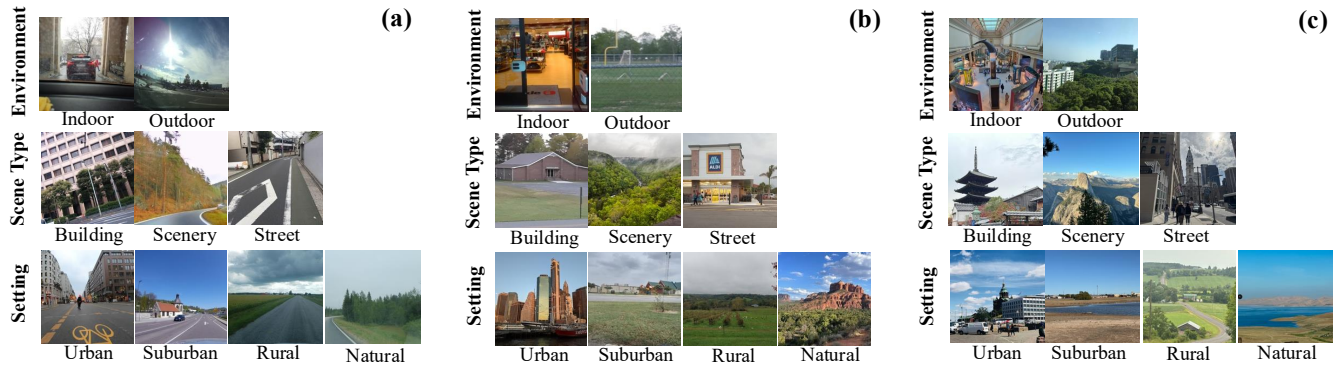


Figure 7: Sample images from the benchmark datasets: (a) Dataset-GSS; (b) Dataset-CUS; (c) Dataset-PCW.

Prompt design for image geolocation.

```

1  SYSTEM_PROMPT = "You are an AI assistant specialized in
2  geocoding analysis from images."
3
4  IMAGE_LOCATION_PROMPT =
5  You are given an image. Use a step-by-step
6  (chain-of-thought) reasoning process to infer the
7  most likely location.
8
9  Structure your response in three sections:
10 1. **Image Information** - Describe the general setting of
11  the image.
12 2. **Reasoning** - Provide detailed justifications using
13  observable visual cues.
14 3. **image geolocation** - Output your best-guess
15  location with a confidence score.
16
17 Your response must be valid JSON in this exact format:
18 { "image_information": {
19   "environment": "indoor|outdoor",
20   "scene_type": "building|scenery|street|mixed",
21   "setting": "urban|suburban|rural|natural"},
22  "reasoning": {
23   "landmark_recognition": "e.g., iconic structures,
24   architectural landmarks, natural features",
25   "text_and_signage": "e.g., street signs, business
26   names, license plates, visible text",
27   "cultural_indicators": "e.g., architectural styles,
28   regional patterns, cultural elements",
29   "spatial_context": "e.g., geographic relationships,
30   infrastructure patterns"},
31  "reverse_geocoding": {
32   "confidence": "1|2|3|4|5",
33   "address": {
34     "street": "street address",
35     "city": "city name",
36     "state": "state/province",
37     "country": "country name"},
38   "coordinates": {
39     "latitude": "decimal degrees",
40     "longitude": "decimal degrees"}}}
41
42 Example:
43 { "image_information": {
44   "environment": "outdoor",
45   "scene_type": "building",
46   "setting": "urban"},
47  "reasoning": {
48   "landmark_recognition": "Empire State Building
49   with distinctive Art Deco spire clearly visible",
50   "text_and_signage": "NYC taxi markings
51   and New York license plates",
52   "cultural_indicators": "Dense Manhattan urban
53   layout with characteristic skyscraper arrangement",
54   "spatial_context": "Midtown Manhattan street grid
55   and building density patterns"},
56  "reverse_geocoding": {
57   "confidence": "5",
58   "address": {
59     "street": "350 5th Ave",
60     "city": "New York",
61     "state": "NY",
62     "country": "USA"},
63   "coordinates": {
64     "latitude": "40.7484",
65     "longitude": "-73.9857"}}}
66
67 Guidance:
68 - Return only valid JSON, no additional text
69 - Return a confidence score between 1 (low) and 5 (high)
70 - For image geolocation, return only one
71 location that you are mostly confident

```

Figure 8: Prompt used to elicit structured geolocation reasoning and prediction from LLMs.

edge over open-source alternatives. This time, however, o3 achieves the highest city-level accuracy at 60.8%, closely followed by gpt-4.1 at 60.0%, while gemini-2.5-pro displays precision with the lowest median distance error of 0.7 km. In contrast, open-source models continue to lag behind: llama-4-17b and llama-3.2-11b reach only 40.8% and 41.9% city-level accuracy, respectively, with higher median errors of 34.3 km and 10.5 km.

Similarly, the computational cost analysis mirrors earlier patterns. While llama-3.2-11b offers the most cost-effective solution at \$0.00014 per request with only 783 average tokens, this efficiency comes at the expense of reduced accuracy. Conversely, o3 delivers superior performance but at a premium cost of \$0.01117 per request. Among the models, gemini-1.5-pro and gemini-2.5-flash show competitive performance (54.4% city accuracy, 1.5 km median

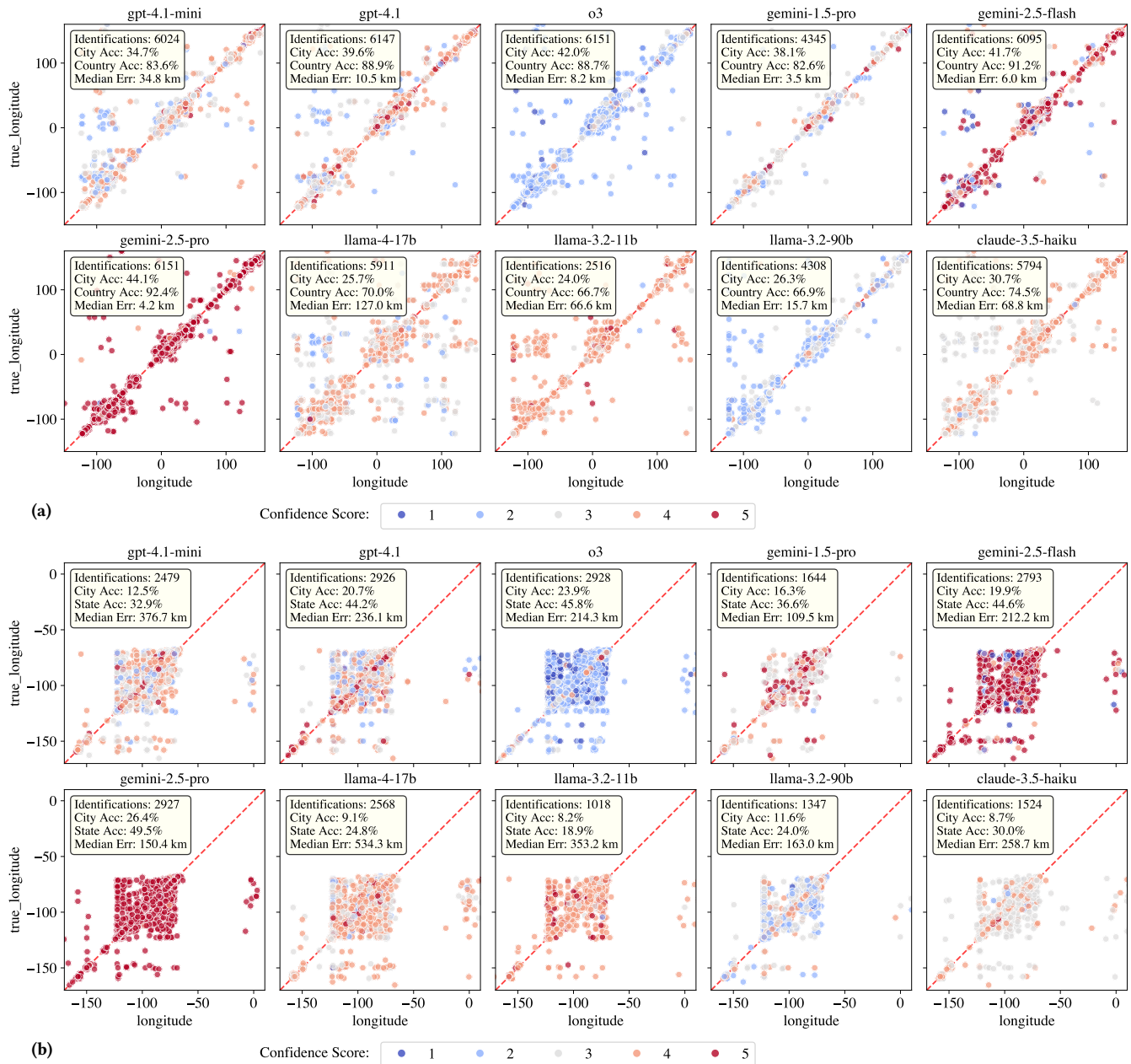


Figure 9: Benchmark performance based on longitude prediction. (a) Dataset-GSS, and (b) Dataset-UPC. Perfect predictions lie on the red dashed diagonal line. The proximity of points to this line indicates the model’s accuracy, with the color of each point representing the model’s self-reported confidence score on a scale of 1 to 5.

error) with relatively efficient resource use (1,180 tokens, \$0.00244 per request). These findings show that while larger models often perform better, the trade-off between model size, cost, and accuracy remains nuanced for practical use cases.

F Extended Feature Attribution Results

We perform a post-hoc diagnostic to quantify how well each model’s own extracted semantic fields predict its success or failure. For each model, we regress its city-level prediction correctness (binary) and its log-transformed distance error (continuous) against these four fields using logistic and ridge regression. Results are reported on all three benchmark splits.

Table 4: LLM performance benchmark based on Dataset-PCW.

Model	City Acc (%)	Country Acc (%)	Median Dist (km)	Avg Tokens	Avg Cost (\$)
gpt-4.1-mini	51.8%	95.3%	2.9	3041	.00153
gpt-4.1	60.0%	97.7%	1.4	1621	.00476
o3	60.8%	96.9%	0.9	2350	.01117
gemini-1.5-pro	54.4%	93.3%	1.5	1180	.00244
gemini-2.5-flash	50.2%	96.3%	1.9	1346	.00133
gemini-2.5-pro	58.7%	97.0%	0.7	1345	.00534
llama-4-17b	40.8%	93.4%	34.3	2823	.00089
llama-3.2-11b	41.9%	89.4%	10.5	783	.00014
llama-3.2-90b	50.0%	89.7%	1.9	6848	.00822
claude-3.5-haiku	42.0%	94.1%	10.0	2350	.00266

Table 5: Field-driven performance on Dataset-GSS.

Model	Accuracy \uparrow	AUC \uparrow	MAE _{log} \downarrow	R ² \uparrow
gpt-4.1-mini	0.691	0.736	0.761	0.102
gpt-4.1	0.680	0.753	0.644	0.133
o3	0.707	0.777	0.633	0.141
gemini-1.5-pro	0.635	0.682	0.585	0.099
gemini-2.5-flash	0.699	0.760	0.575	0.165
gemini-2.5-pro	0.691	0.742	0.547	0.171
llama-4-17b	0.733	0.738	1.008	0.091
llama-3.2-11b	0.667	0.617	1.013	0.085
llama-3.2-90b	0.647	0.667	0.763	0.108
claude-3.5-haiku	0.676	0.747	0.836	0.140

Table 6: Field-driven performance on Dataset-UPC.

Model	Accuracy \uparrow	AUC \uparrow	MAE _{log} \downarrow	R ² \uparrow
gpt-4.1-mini	0.852	0.695	0.926	0.083
gpt-4.1	0.793	0.739	0.908	0.177
o3	0.778	0.737	0.920	0.176
gemini-1.5-pro	0.755	0.681	0.834	0.030
gemini-2.5-flash	0.801	0.685	0.888	0.129
gemini-2.5-pro	0.759	0.687	0.874	0.159
llama-4-17b	0.897	0.686	1.030	0.053
llama-3.2-11b	0.858	0.666	1.015	0.071
llama-3.2-90b	0.759	0.689	1.029	0.087
claude-3.5-haiku	0.842	0.713	0.942	0.051

Table 7: Field-driven performance on Dataset-PCW.

Model	Accuracy \uparrow	AUC \uparrow	MAE _{log} \downarrow	R ² \uparrow
gpt-4.1-mini	0.741	0.765	0.735	0.200
gpt-4.1	0.727	0.756	0.551	0.282
o3	0.742	0.770	0.541	0.271
gemini-1.5-pro	0.703	0.750	0.477	0.089
gemini-2.5-flash	0.757	0.790	0.630	0.244
gemini-2.5-pro	0.752	0.787	0.559	0.238
llama-4-17b	0.684	0.770	0.951	0.119
llama-3.2-11b	0.676	0.737	0.959	0.104
llama-3.2-90b	0.771	0.824	0.495	0.389
claude-3.5-haiku	0.766	0.833	0.783	0.217

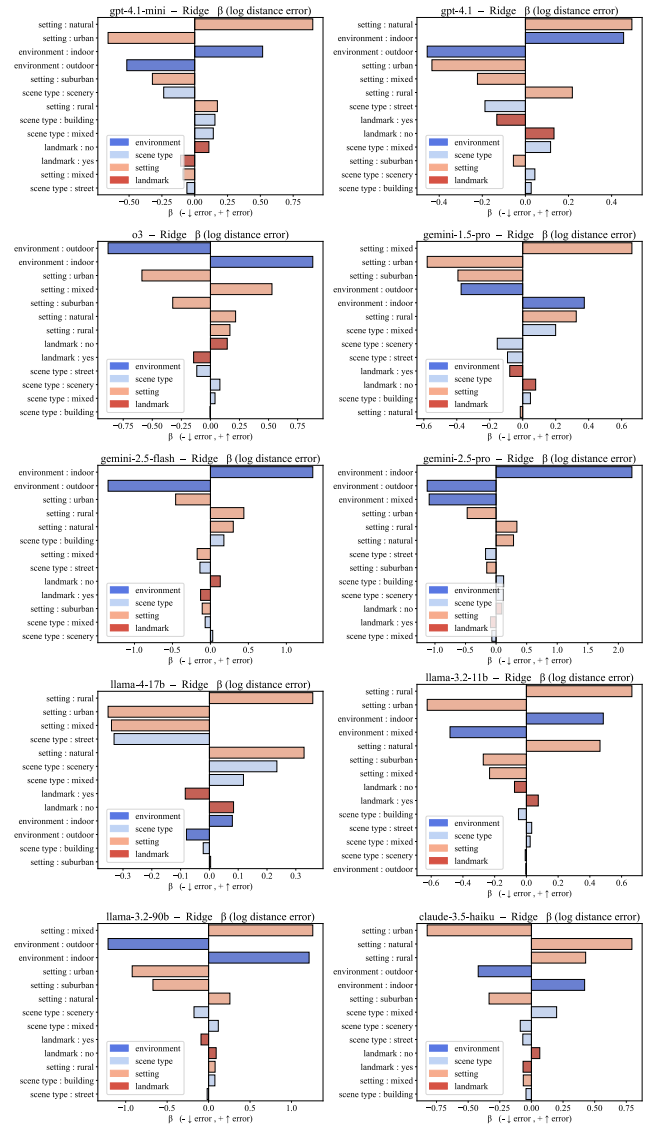


Figure 10: Ridge regression coefficients on Dataset-GSS, using log-distance error as the response. Negative values indicate cues that decrease error; positive values indicate cues that increase error.

This diagnostic analysis reveals how effectively current models ground their geolocation predictions in structured semantic cues, offering insight into their underlying visual-geospatial reasoning capabilities. On Dataset-GSS, which primarily features outdoor urban scenes rich in spatial context, models exhibit stronger alignment between their predicted semantic fields and their final performance. Regression models based on these four elements (environment, scene type, setting, and landmark) explain up to 17% of the variance in log-distance error (R²), with gemini-2.5-pro consistently leading in both interpretability and precision. Its ability to generate semantically rich, spatially aligned tags translates into the lowest MAE_{log} and the highest R², suggesting a high degree of internal consistency between scene understanding and coordinate prediction. In contrast, although llama-4-17b achieves the highest

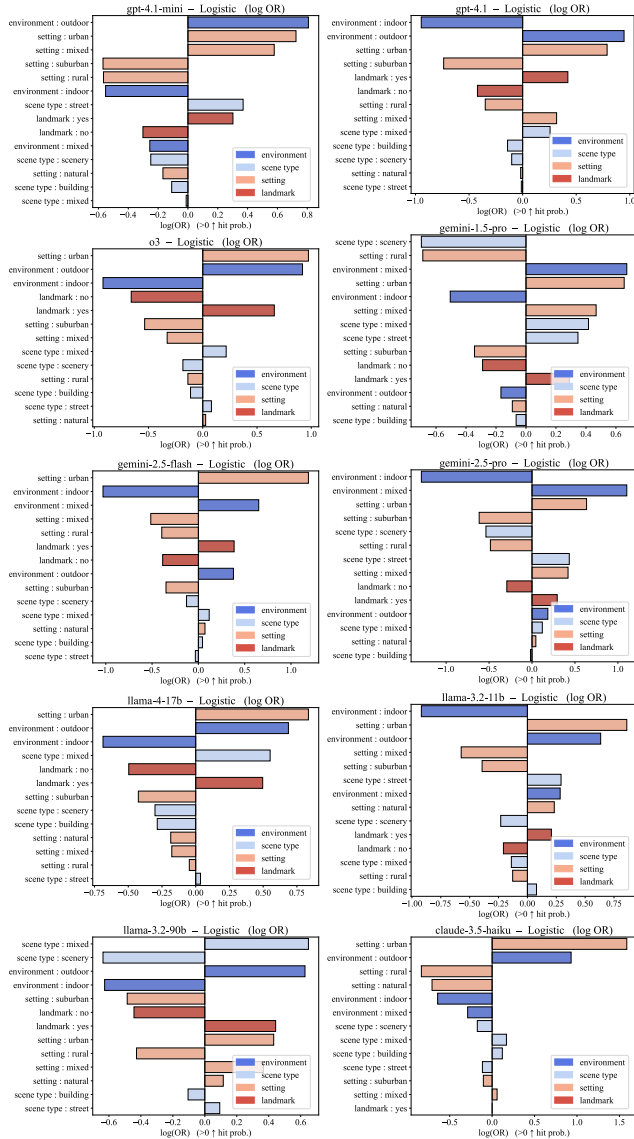


Figure 11: Log-odds coefficients from diagnostic logistic regression on Dataset-UPC. Positive values increase the likelihood of correct city prediction; negative values decrease it.

city-level classification accuracy on both Datasets-GSS and -UPC, its large distance errors indicate that these correct predictions may stem from over-reliance on salient, shortcut features—such as recognizable logos or architectural patterns—without engaging in deeper spatial reasoning or refinement.

The diagnostic further underscores the challenges posed by visually sparse or ambiguous environments. On Dataset-UPC, where scenes (e.g., indoors, signage fragments) often lack distinct geographic structures, field-based regressions degrade sharply across all models. In particular, llama-3.2-90b demonstrates that large open-weight models can internalize meaningful spatial priors when appropriately scaled and tuned, achieving high accuracy and strong R^2 in PCW. Still, the overall explanatory power of these four fields

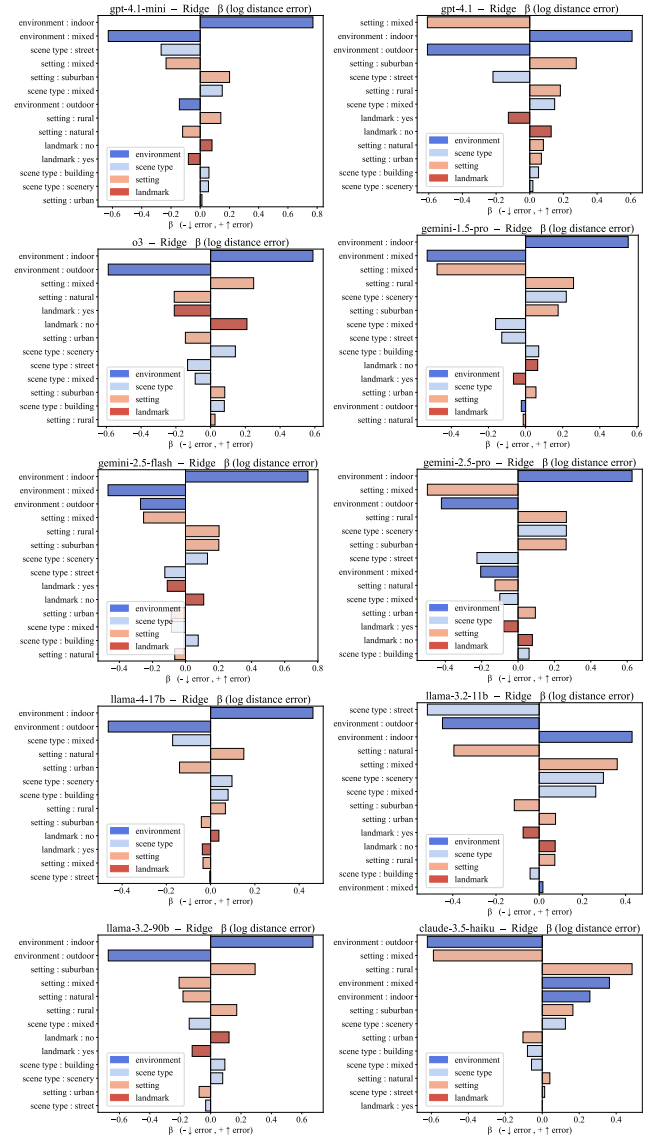


Figure 12: Ridge regression coefficients on Dataset-UPC, using log-distance error as the response. Negative values indicate cues that decrease error; positive values indicate cues that increase error.

remains limited: Even in the best case, the variance in distance errors over 60% remains unaccounted for. This gap suggests that high-level tags like “rural” or “landmark” only scratch the surface of the complex reasoning chain needed for accurate localization. Finer-grained semantics, such as regional architecture, vegetation type, textual cues, and spatial layout, are likely necessary to capture how LLMs reason about place fully.

Figure 10 displays the ridge-regression coefficients for the four semantic fields on Dataset-GSS, with the log-distance error as the dependent variable. Each bar shows the directional contribution of a cue: larger negative values (left of the axis) correspond to stronger error reduction, whereas positive values indicate error amplification. Among all cues, setting and environment are the

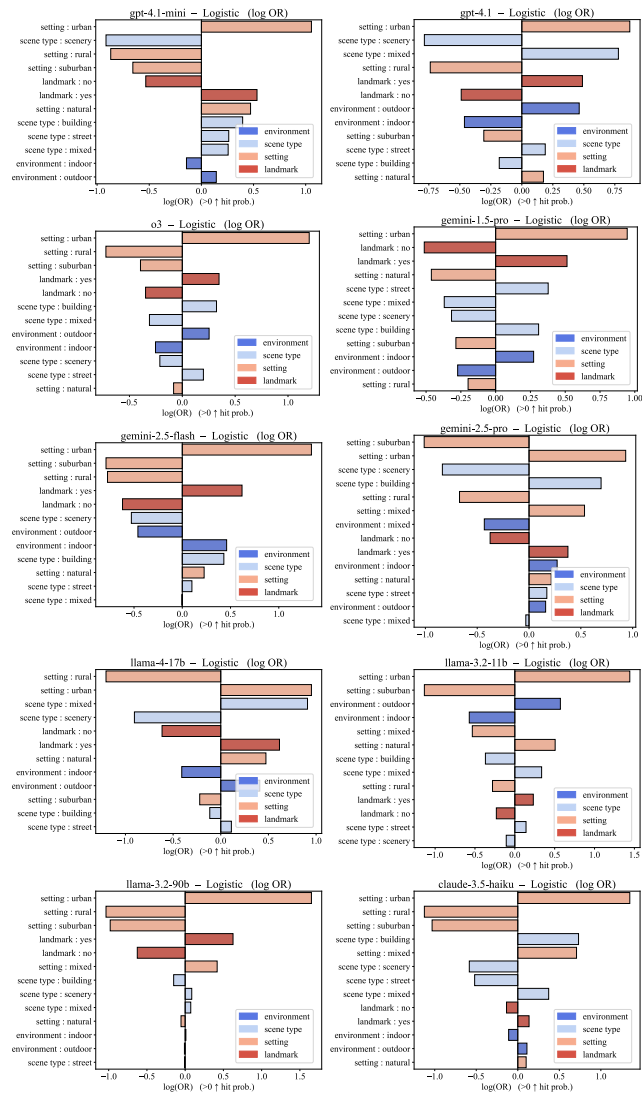


Figure 13: Log-odds coefficients from diagnostic logistic regression on Dataset-PCW. Positive values increase the likelihood of correct city prediction; negative values decrease it.

most influential. Outdoor scenes receive the most negative weights, confirming that external spatial anchors (skylines, road geometry, and signage) can substantially improve geolocation prediction. By contrast, indoor scenes attract large positive weights (notably for gemini-2.5-pro), underscoring how precision degrades once exterior context is lost. The setting field exhibits a similar polarity: urban imagery lowers error, whereas rural or natural settings raise it. This likely reflects biases in several models training data, which may overrepresent urban environments and their characteristic spatial patterns such as grid layouts or dense built form.

Figures 11–14 extend this analysis to Dataset-UPC and Dataset-PCW. On UPC, the predictive power of semantic fields declines sharply: R^2 values drop and landmark coefficients collapse toward zero, indicating reduced access to external anchors. On PCW, open-weight models like llama-3.2-90b show strong negative weights

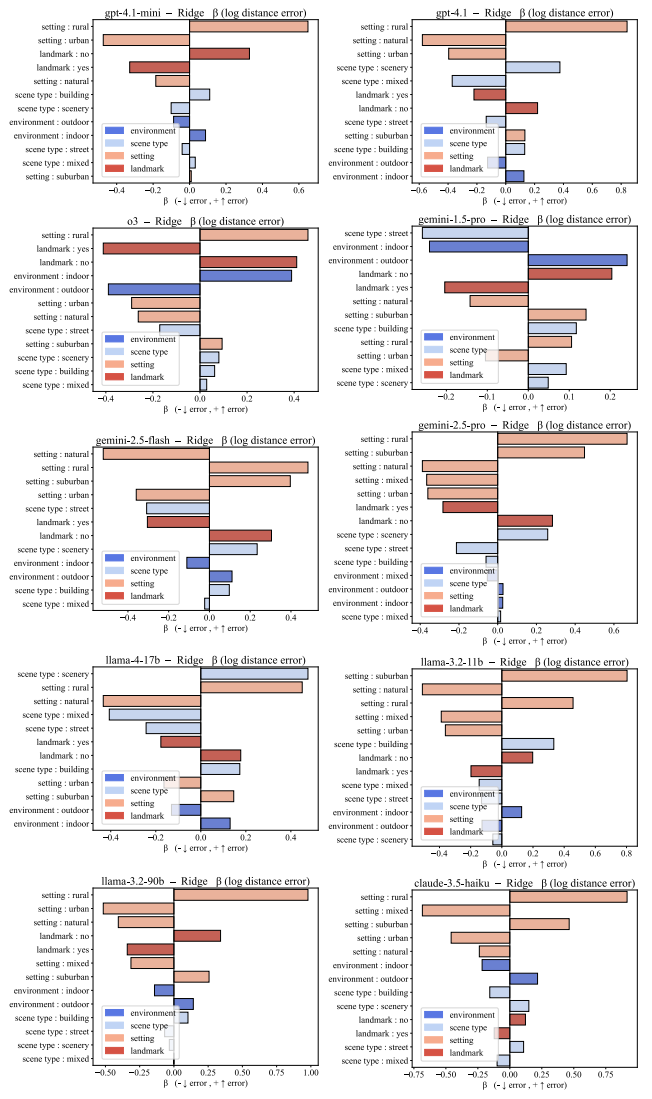


Figure 14: Ridge regression coefficients on Dataset-PCW, using log-distance error as the response. Negative values indicate cues that decrease error; positive values indicate cues that increase error.

for urban and outdoor cues (corresponding to the highest R^2 on this split), but also greater variance, with large positive weights for ambiguous scene types such as buildings or scenery. In contrast, proprietary models like gemini-2.5-pro and o3 adopt flatter, more conservative profiles, yielding fewer high-confidence errors. Overall, model performance peaks when scenes are urban, outdoor, and landmark-rich, but degrades rapidly under distribution shift.

G Extended Word-Cloud Analysis

Figure 15 presents the word clouds for the nine remaining models. First, most models rely on traffic-related terms such as “sign,” “street,” and “road.” This common vocabulary highlights a general model preference for OCR-visible and regulation-focused features, especially both gpt-4.1 and gpt-4.1-mini prominently feature these

Table 8: Representative LLM image geolocalization output in Dataset-GSS.

Image	Ground-Truth	LLM Output
	Address: Jakarta, Indonesia Coordinates: -6.2088, 106.8459	Model: gemini-2.5-pro environment: outdoor scene_type: street setting: urban landmark_recognition: The tall, light-colored residential building visible in the background is the Permata Senayan apartment complex in Jakarta. text_and_signage: Multiple road signs are visible in Indonesian. The most prominent yellow sign reads "Hati - Hati Lintasan Bus Transjakarta," which translates to "Be Careful, Transjakarta Bus Crossing." Another sign below it reads "HATI-HATI PORTAL BUSWAY." Transjakarta is the Bus Rapid Transit (BRT) system exclusive to Jakarta, Indonesia. A vehicle license plate starting with the letter 'B' is also partially visible, which is the vehicle registration code for the Jakarta metropolitan area. cultural_indicators: The language on the signs is Indonesian. The high density of traffic, including numerous motorcycles, is characteristic of major cities in Indonesia, particularly Jakarta. spatial_context: The scene depicts a crossing for a dedicated busway. The combination of the specific sign configuration, the location of the Permata Senayan apartment building in the background, the fence on the right (belonging to the Gelora Bung Karno complex), and the orientation of the road points directly to Jalan Tentara Pelajar, near the Palmerah railway station in Central Jakarta. The camera is facing southeast along this road. Confidence: 5 Address: Jalan Tentara Pelajar, Jakarta, JAKARTA, Indonesia Coordinates: -6.2117, 106.7977
	Address: Paris, France Coordinates: 48.8523, 2.3541	Model: o3 environment: outdoor scene_type: street setting: urban landmark_recognition: Haussmann-style cream stone buildings with wrought-iron balconies typical of central Paris streets; red café awnings common on well-known pedestrian market streets such as Rue Cler. text_and_signage: Word "CAFÉ" in French clearly visible on red awning; menu board beside wooden café frontage also in French. cultural_indicators: Parisian sidewalk-café culture, narrow cobble roadway shared by pedestrians, architectural moldings and window shutters characteristic of late-19th-century Paris buildings. spatial_context: Pedestrian market street lined with small shops, cafés, and outdoor produce stalls matches the layout of the 7th-arrondissement market street Rue Cler located between Avenue de la Motte-Picquet and Rue de Grenelle. Confidence: 3 Address: Rue Cler, Paris, ILE-DE-FRANCE, France Coordinates: 48.8569, 2.3062
	Address: Shoreline, USA Coordinates: 47.7633, -122.3239	Model: gemini-2.5-pro environment: outdoor scene_type: street setting: suburban landmark_recognition: The primary landmarks are the highway infrastructure itself, including a multi-lane freeway, an overpass, and large overhead gantry signs. The presence of tall evergreen trees is characteristic of the Pacific Northwest region of the United States. text_and_signage: Multiple highway signs are clearly visible. One sign indicates 'EXIT 176' for 'NE 175th St' and 'Shoreline' is 1/2 mile ahead. Another sign lists upcoming exits and their distances: 'NE 145th St' (2 miles), 'Northgate Way' (3 1/4 miles), and 'N 85th St' (5 miles). These exits, street names, and locations (Shoreline, Northgate) are all situated along Interstate 5 in the northern part of Seattle and its immediate suburbs in Washington State. cultural_indicators: The style of the green highway signs with white text (Highway Gothic font) conforms to the Manual on Uniform Traffic Control Devices (MUTCD) used in the United States. The use of 'miles' for distance measurement is standard in the US. spatial_context: The image is taken from a vehicle traveling northbound on a major freeway. The exit numbers and destinations confirm the location is on Interstate 5 (I-5) North. Specifically, the signs for Exit 176 (NE 175th St) being 1/2 mile away, and being mounted on an overpass, place the camera's location just south of the NE 185th St overpass in Shoreline, Washington, looking north. Confidence: 5 Address: Interstate 5 N, Shoreline, WA, USA Coordinates: 47.7592, -122.3293
	Address: Hildesheim, Germany Coordinates: 52.1528, 9.9359	Model: o3 environment: outdoor scene_type: street setting: suburban landmark_recognition: No globally iconic landmark visible; single-family house with red tile roof and fenced yard on right side. text_and_signage: Large white construction-information board on the left shows an EU flag logo and multi-line text typical of EU-funded public works signs in Germany; road signs are European style (red-bordered triangular warning sign, round red-bordered 30 km/h speed limit, blue shared-path sign). cultural_indicators: Red/grey concrete block sidewalk with integrated cycle lane, metal mesh fencing, and the specific designs of the traffic signs match common German street infrastructure; house architecture (white stucco, steep red clay roof) also typical for central Germany. spatial_context: Two-lane road with modest traffic, greenery and detached housing indicate a suburban area on the edge of a medium/large German city. Confidence: 2 Address: Berliner Straße, Potsdam, BRANDENBURG, Germany Coordinates: 52.4000, 13.0400
	Address: Riga, Latvia Coordinates: 56.9492, 24.1100	Model: gemini-2.5-pro environment: outdoor scene_type: street setting: urban landmark_recognition: The architecture is characteristic of a Northern or Eastern European old town, specifically the Hanseatic style found in the Baltic states. The pink building at the end of the street with a stepped gable is a distinctive local landmark. text_and_signage: A crucial clue is the text 'BERGA FASADES' visible on the gable of the pink building. 'Fasādes' is the Latvian word for 'facades'. Below the windows on the same building, the word 'RESTORANS' (Latvian for 'restaurant') can be faintly seen. These linguistic cues definitively point to Latvia. cultural_indicators: The cobblestone street, the style of the buildings, and the general atmosphere are highly indicative of the Old Town (Vecrīga) in Riga, Latvia. The presence of numerous outdoor cafes is also typical for this historic tourist area. spatial_context: The photograph is taken looking down a narrow, pedestrianized street. By cross-referencing the building with 'BERGA FASADES' with maps of Riga, the location is identified as Tirgoņu iela, looking towards the intersection with Šķūņu iela. Confidence: 5 Address: Tirgoņu iela, Riga, RIGA, Latvia Coordinates: 56.9479, 24.1084
	Address: Cainta, Philippines Coordinates: 14.5765, 121.1261	Model: o3 environment: outdoor scene_type: street setting: urban landmark_recognition: No globally iconic landmark visible; scene shows small shops and residential structures typical of Southeast Asian urban neighborhoods. text_and_signage: English construction warning signs such as 'DANGER DRILLING IN PROGRESS' and 'THIS PROJECT WILL BENEFIT THE ...' plus campaign-style posters with English names (e.g., 'BEN') suggest the Philippines where English is an official language used in public signage. cultural_indicators: Dense overhead utility wires, jeepney-sized blue mini-truck, tropical coconut palm, concrete block houses with metal window grilles, and roadside sari-sari-store style stalls strongly resemble streets in Philippine barangays. spatial_context: Narrow two-way lane lined with stalls and residences, temporary construction barriers, and cluttered electrical infrastructure typical of inner neighborhoods in Metro Manila cities such as Quezon City. Confidence: 3 Address: Quezon City, METRO MANILA, Philippines Coordinates: 14.6500, 121.0500
	Address: Echternach, Luxembourg Coordinates: 49.8355, 6.3285	Model: o3 environment: outdoor scene_type: scenery setting: rural landmark_recognition: No globally iconic landmark visible; scene shows a forested footpath descending toward a plaster-walled house with a steep roof typical of Central European villages. text_and_signage: No readable text or signage present. cultural_indicators: Green-painted metal handrail, English ivy climbing conifer and deciduous trunks, and pastel stucco house are characteristic of small towns in western Germany's river valleys (e.g., Mosel/Rhine). spatial_context: Path on a wooded hillside suggests settlements nestled in narrow valleys; common in Rhineland-Palatinate where towns sit between steep, forested slopes and rivers. Confidence: 2 Address: Moselpromenade 1, Cochem, RHINELAND-PALATINATE, Germany Coordinates: 50.1453, 7.1656

Table 9: Representative LLM image geolocalization output in Dataset-UPC.

Image	Ground-Truth	LLM Output
	Address: Philadelphia, USA Coordinates: 39.9531, -75.1635	Model: o3 environment: outdoor scene_type: building setting: urban landmark_recognition: Ornate Second-Empire style municipal building with a central clock tower topped by a statue, matching the well-known Philadelphia City Hall and its William Penn statue text_and_signage: No readable signage visible but the clock face and tower design are distinctive enough for identification cultural_indicators: Presence of both English and Chinese text matches Honolulu Chinatown area; tropical plants and palms fit Hawaiian climate spatial_context: Street-level retail space in a mid-rise urban block typical of downtown Honolulu near Queen Emma Street corridor Confidence: 4 Address: 1280 Queen Emma Street, Honolulu, HI, USA Coordinates: 21.3148, -157.8576
	Address: Bristol, CT Coordinates: 41.6796, -72.9408	Model: gemini-2.5-pro environment: outdoor scene_type: building setting: suburban landmark_recognition: The main building is the American Clock & Watch Museum, a specific cultural landmark. An ornate street clock is also visible on the left side of the property. text_and_signage: A large sign in the foreground and a smaller sign on the building itself clearly read 'AMERICAN CLOCK & WATCH MUSEUM'. cultural_indicators: The building exhibits a classic American Colonial architectural style, characterized by its white clapboard siding, symmetrical facade, and multi-pane sash windows, which is very common in the New England region of the United States. spatial_context: The image shows a large historic house set back from a road with a lawn in front, next to a smaller, attached building and a parking area, which is consistent with the layout of a museum in a suburban or small-town setting. Confidence: 5 Address: 100 Maple St, Bristol, CT, USA Coordinates: 41.6766, -72.9461
	Address: Norfolk, NE Coordinates: 42.0158, -97.4102	Model: gemini-2.5-pro environment: indoor scene_type: building setting: urban landmark_recognition: The most significant visual feature is the ceiling and upper walls being completely covered in autographed US dollar bills. This is a distinctive tradition of a limited number of bars in the United States, making it a key identifying feature. text_and_signage: Several crucial pieces of text are visible. A sign on the lower right, partially obscured, reads 'THE MINT BAR'. A second sign, located under a television on the left side, says 'UNION BAR'. The combination of a bar featuring both 'Union Bar' and 'The Mint Bar' names, along with the dollar bill decor, is highly specific. A large white flag with a blue 'W' is prominently displayed, which is the victory flag for the Chicago Cubs baseball team. While this could be found in many bars, it fits the context of a Midwestern location. Other text on dollar bills like 'COLORADO' and 'BAYTOWN' are likely from visitors and less indicative of the primary location. cultural_indicators: The tradition of pinning signed currency to the walls is a cultural practice in some American saloons and dive bars, often accumulating over many decades. The Chicago Cubs 'W' flag is a strong element of American sports culture, particularly in the Midwest. The green, shamrock-shaped string lights suggest an Irish pub theme or St. Patrick's Day decorations, common in American bars. spatial_context: The sheer density of the currency covering almost every available surface suggests this is a very old, long-standing tradition at this establishment. This points towards a historic local bar rather than a new or chain establishment. A search for bars with these specific features (dollar bills, 'Union Bar', 'The Mint Bar') confirms the identity of a well-known location in Nebraska. Confidence: 5 Address: 1401 10th St, Gering, NE, USA Coordinates: 41.8242, -103.6625
	Address: Portage, IN Coordinates: 41.5583, -87.1814	Model: gemini-2.5-pro environment: outdoor scene_type: building setting: suburban landmark_recognition: The image features a single-story commercial building with a distinct gabled entrance. The architecture, combining brick, siding, and shingled roofing, is common for suburban medical or professional offices in the United States. text_and_signage: A prominent sign is visible on the building's facade. The sign includes a logo with the name 'Porter' and text that reads 'CENTER FOR SLEEP MEDICINE' and 'REHABILITATION SERVICES'. This information is key to identifying the specific business and its location. cultural_indicators: The building style, the presence of a large asphalt parking lot, and the manicured grass strip are all characteristic of suburban development patterns in North America. spatial_context: A search for 'Porter Center for Sleep Medicine & Rehabilitation Services' leads to Northwest Health - Porter facilities in Indiana. Using Google Maps and Street View, the building in the image is an exact match for the one located at 2000 Roosevelt Rd in Valparaiso, IN. The building's structure, sign placement, and surrounding features align perfectly with online imagery of this address. Confidence: 5 Address: 2000 Roosevelt Rd, Valparaiso, IN, USA Coordinates: 41.4880, -87.0545
	Address: Biloxi, MS Coordinates: 30.4461, -88.9394	Model: o3 environment: outdoor scene_type: building setting: suburban landmark_recognition: No globally iconic landmark, but the facade resembles mid-1990s–2000s U.S. suburban office-park architecture (stucco/EIPS, shallow arch window tops, square columns). text_and_signage: The only visible text is the street number '1721' mounted on the entrance canopy. cultural_indicators: Presence of large live-oak trees, beige stucco, and green-tinted ribbon windows strongly suggest a warm southern-U.S. region, particularly Texas where this design and vegetation are common. spatial_context: Looks like a stand-alone low-rise in an office park surrounded by mature trees rather than dense urban grid. Confidence: 2 Address: 1721 River Run, Fort Worth, TX, USA Coordinates: 32.7362, -97.3620
	Address: Bay Village, OH Coordinates: 41.4794, -81.8815	Model: gemini-2.5-pro environment: outdoor scene_type: mixed setting: suburban landmark_recognition: The primary identifying feature is the unique circular monkey bar structure, known as a 'RingTrek' climber. The scene also includes adjacent tennis courts with green surfaces and a chain-link fence, a swing set with distinctive beige bucket-like seats, and a small play structure with a green hexagonal roof. The specific combination and arrangement of this playground equipment are highly distinctive. text_and_signage: A brown sign is visible on a post, likely a standard park rules sign, but the text is illegible and does not contribute to the identification. cultural_indicators: The style of the playground equipment is common in modern North American public parks. The houses visible in the background are of a typical suburban American design. spatial_context: The layout of a playground directly adjacent to tennis courts, bordered by trees and with residential housing in the near distance, is a common configuration for a community park in the United States. The deciduous trees suggest a temperate climate. Confidence: 5 Address: Continental Pl, Glen Cove, NY, USA Coordinates: 40.8529, -73.6338
	Address: Colby, KS Coordinates: 39.2779, -100.9437	Model: gemini-2.5-pro environment: outdoor scene_type: scenery setting: rural landmark_recognition: The central feature is a small, yellow statue of a monkey-like figure in a raincoat. This is a known, unique roadside attraction called the 'I-80 Rainslicker Monkey' or 'Monkey Tree', which serves as an informal memorial. text_and_signage: In the background, on top of the grassy embankment, there are road signs. A cropped image clearly shows a US Interstate shield for Interstate 80 (I-80) and a US Highway shield for US Route 30 (US-30). These two highways run concurrently in this region. cultural_indicators: The object is a small, informal roadside memorial, a cultural practice found along highways in the United States, often maintained by locals to commemorate an event or person. spatial_context: The image is taken from a low vantage point looking up at a grassy embankment next to a major highway. The presence of both I-80 and US-30 signs, combined with the rolling, grassy, and sparsely populated landscape, is characteristic of southern Wyoming. Confidence: 5 Address: Interstate 80, Buford, WY, USA Coordinates: 41.2251, -105.4242

Table 10: Representative LLM image geolocalization output in Dataset-PCW.

Image	Ground-Truth	LLM Output
	Address: Philadelphia, USA Coordinates: 39.9531, -75.1635	Model: o3 environment: outdoor scene_type: building setting: urban landmark_recognition: Ornate Second-Empire style municipal building with a central clock tower topped by a statue, matching the well-known Philadelphia City Hall and its William Penn statue text_and_signage: No readable signage visible but the clock face and tower design are distinctive enough for identification cultural_indicators: French Second-Empire architecture common to late-19th-century U.S. civic buildings, specifically the gray granite and elaborate sculptural ornamentation characteristic of Philadelphia City Hall spatial_context: Large civic structure occupying a city square in the heart of a dense downtown grid, consistent with Center City Philadelphia where City Hall sits at the crossing of Broad and Market Streets confidence: 5 address: 1400 John F Kennedy Blvd, Philadelphia, PA, USA coordinates: 39.9526, -75.1636
	Address: Mackinaw City, USA Coordinates: 45.8388, -84.7209	Model: Gemini-2.5-pro environment: outdoor scene_type: scenery setting: natural landmark_recognition: The central feature of the image is a very large, illuminated suspension bridge at night. The design, with its two prominent lighted towers and extensive truss structure, is unmistakably the Mackinac Bridge, which connects the Upper and Lower Peninsulas of the U.S. state of Michigan. Additionally, a faint green glow of the aurora borealis (Northern Lights) is visible in the sky, a phenomenon often observed in this northern region. text_and_signage: There is no legible text or signage visible in the image. cultural_indicators: The scale and style of the bridge are characteristic of major mid-20th century American civil engineering projects. The presence of the aurora suggests a location at a high latitude in the Northern Hemisphere. spatial_context: The photograph is taken from a sandy and pebbly beach, looking across a large body of water (the Straits of Mackinac) towards the bridge. The angle of the bridge suggests the photo was taken from the southern side, in Mackinaw City, looking north/northeast. A popular and accessible viewing spot with this perspective is Alexander Henry Park, located just west of the bridge's southern approach. confidence: 5 address: Alexander Henry Park, Mackinaw City, MI, USA coordinates: 45.782, -84.7334
	Address: Lubbock, USA Coordinates: 33.5162, -101.919	Model: o3 environment: outdoor scene_type: scenery setting: suburban landmark_recognition: No globally iconic landmark; scene shows a man-made pond or small lake with bald cypress trees that commonly line park lakes in the southern United States. text_and_signage: No readable text or signage visible in the image. cultural_indicators: Dormant warm-season grass and bald cypress suggest a warm climate that still experiences a cool season; this combination is common in North Texas municipal parks. spatial_context: Flat terrain, scattered single-story buildings/roofs and a roadway in the distance imply a suburban park setting rather than an isolated rural lake or dense urban waterfront. confidence: 2 address: 1405 Wilson Creek Pkwy, McKinney, TX, USA coordinates: 33.1974, -96.6232
	Address: Tampa, USA Coordinates: 28.1284, -82.368	Model: Gemini-2.5-pro environment: outdoor scene_type: street setting: suburban landmark_recognition: The image features storefronts in a modern suburban shopping plaza, not a unique landmark, but characteristic of this type of development. text_and_signage: Multiple signs are clearly visible. The main storefronts are for 'COLD STONE CREAMERY' and 'PARIS BAGUETTE'. Crucially, the street number '17519' is displayed on a pillar at the entrance of the Cold Stone Creamery. A poster in the window also provides a URL: www.ColdStoneCakes.com, which is a US-based domain. cultural_indicators: The architectural style of the buildings is typical of contemporary American suburban retail centers or strip malls. The combination of these specific international food chains (Cold Stone Creamery and Paris Baguette) is common in more affluent suburban areas in the United States. spatial_context: The image shows two businesses located directly next to each other in a shopping center. The combination of Cold Stone Creamery, Paris Baguette, and the specific address number '17519' provides a unique set of data points to query for a specific location. confidence: 5 address: 17519 W Colonial Dr, Winter Garden, FL, USA coordinates: 28.552942, -81.564633
	Address: Ann Arbor, USA Coordinates: 42.2991, -83.7129	Model: o3 environment: outdoor scene_type: scenery setting: suburban landmark_recognition: No clearly identifiable landmark; landscape of mixed deciduous and coniferous trees with a small glimpse of a red-brick building typical of Midwestern college campuses text_and_signage: No readable street signs, business names, or license plates visible cultural_indicators: Streetlights with simple black curved arms and a red fire-hydrant are common municipal furnishings in many U.S. northern cities; red-brick institutional building hints at a school or campus built mid-20th-century, often found in the Upper Midwest spatial_context: Lightly trafficked two-lane road inside a landscaped area, snow cover, and dense spruce/pine mix are consistent with cities along Lake Superior such as Duluth, Minnesota confidence: 2 address: University Drive, Duluth, MN, USA coordinates: 46.8185, -92.0844
	Address: Mount Vernon, USA Coordinates: 38.7082, -77.087	Model: o3 environment: outdoor scene_type: mixed setting: rural landmark_recognition: Formal, walled kitchen garden (potager) with espaliered fruit trees and neat vegetable beds; small ancillary buildings with steep red-tile roofs and dormer windows suggest 17th-18th-century French estate outbuildings text_and_signage: No readable signage or text visible cultural_indicators: Clay-tile roofing, cream masonry walls, symmetrical dormers and the very structured 'potager' layout are typical of historic French châteaux estates, especially the Potager du Roi built for Louis XIV near Versailles spatial_context: Garden enclosed by low walls, outbuildings just inside, wide sky and distant tree line hint at location on slightly elevated plateau much like the Royal Kitchen Garden site south of the Palace of Versailles confidence: 2 address: 10 Rue du Maréchal Joffre, Versailles, ÎLE-DE-FRANCE, France coordinates: 48.8015, 2.133
	Address: Tulum, Mexico Coordinates: 20.2029, -87.4734	Model: Gemini-2.5-pro environment: outdoor scene_type: building setting: urban landmark_recognition: The location is identified as GITANO Garden of Love in New York City. Distinctive features include a thatched roof over a patio, real tree trunks used as support columns, a prominent disco ball, a gravel floor, and an overall 'jungle chic' or 'Tulum-inspired' aesthetic. text_and_signage: No legible text or signage is clearly visible that aids in identification. A poster on a column is intentionally obscured. cultural_indicators: The decor is highly characteristic of the Gitano brand, which blends a bohemian, jungle-like atmosphere (often associated with Tulum, Mexico) with urban nightlife elements like disco balls and moody lighting. This specific style is a strong cultural indicator for this particular chain of venues. spatial_context: The scene depicts a trendy outdoor bar/restaurant patio, a type of venue common in major urban centers. The specific combination of design elements, including the layout of the patio, the stacked terracotta pots, and the wooden spool table, was matched via comparison with online photos of the identified venue in New York City. confidence: 5 address: 76 Varick Street, New York, NY, USA coordinates: 40.72234, -74.00681
	Address: Mexico Coordinates: 21.0466, -86.793	Model: Gemini-2.5-pro environment: outdoor scene_type: scenery setting: natural landmark_recognition: The dominant natural feature is a dense mangrove forest, characterized by trees with visible prop roots growing directly at the edge of a saltwater or brackish waterway. This type of ecosystem is specific to tropical and subtropical coastlines. text_and_signage: No text or identifiable signage is visible in the image. cultural_indicators: The presence of a recreational watercraft (partially obscured yellow boat, possibly a jet ski or small motorboat) combined with the mangrove environment is very common in the coastal regions of Florida, which has extensive mangrove forests and a large boating culture. spatial_context: The image depicts a coastal inlet or intracoastal waterway. The choppy water and the wake from a boat suggest an active channel used for recreation. This scenery is highly representative of the Intracoastal Waterway in South Florida, particularly in areas like Fort Lauderdale or Miami. confidence: 3 address: Intracoastal Waterway, Fort Lauderdale, FL, USA coordinates: 26.099167, -80.116389